



UNIVERSIDAD DE CHILE
FACULTAD DE CIENCIAS FÍSICAS Y MATEMÁTICAS
DEPARTAMENTO DE GEOFÍSICA

ANÁLISIS DE LA VARIABILIDAD DE CARBONO NEGRO Y OZONO EN CERRO
TOLOLO PARA EL PERIODO 2013-2015

**TESIS PARA OPTAR AL GRADO DE MAGISTER EN METEOROLOGÍA Y
CLIMATOLOGÍA**

PATRICIO ANDRÉS VELÁSQUEZ ÁLVAREZ

PROFESOR GUÍA:
SR. NICOLÁS HUNEEUS LAGOS

COMISIÓN
SR. ROBERTO RONDANELLI ROJAS
SR. NICOLAS BUKOWIECKI

SANTIAGO DE CHILE
2016

**RESUMEN DE TESIS PARA OPTAR AL GRADO DE MAGÍSTER EN
METEOROLOGÍA Y CLIMATOLOGÍA**

**ANÁLISIS DE LA VARIABILIDAD DE CARBONO NEGRO Y OZONO EN
CERRO TOLOLO PARA EL PERIODO 2013-2015**

The global-impact of aerosols on the radiative balance depends on the regional emissions. In view of this, it is necessary to have a look of aerosol optical properties in several places of world. Furthermore, increasing ozone concentrations are observed in the troposphere and their measurements at remote places are keys to assess the impact of the anthropogenic activities. Accordingly, since 1995 watching stations have been installed as part of GAW Program by the WMO. Particularly, in Chile, one of them corresponds to Cerro Tololo (TLL).

Ozone shows high (low) concentrations during afternoon and night (morning), and maximal (minimum) during spring (summer). Their monthly variability is linked to the biomass-burning in the southern hemisphere. Equivalent black carbon shows the same diurnal pattern as ozone, and high (low) concentrations in summer (winter). Their monthly variability is probably related to the human activity in the surrounding valleys. Angstrom exponents show that TLL is influenced by dust and aged diesel soot black carbon rather than biomass-burning emissions.

Air parcels coming from upper-levels, over the ocean and polluted areas are observed at TLL. First parcels represent stratosphere-troposphere interchange. Second parcels represent see-breeze. Finally, third parcels represent local transport from the surrounding areas.

RESUMEN DE TESIS PARA OPTAR AL GRADO DE MAGÍSTER EN METEOROLOGÍA Y CLIMATOLOGÍA

ANÁLISIS DE LA VARIABILIDAD DE CARBONO NEGRO Y OZONO EN CERRO TOLOLO PARA EL PERIODO 2013-2015

El impacto global de los aerosoles en el balance radiativo depende de las emisiones regionales. Por esto es necesario tener una visión de las propiedades ópticas de los aerosoles en muchos lugares del planeta. Además, se ha observado un aumento de las concentraciones de ozono en la tropósfera, cuyas mediciones son fundamental determinando el impacto de las actividades antropogénicas. En consecuencia, estaciones de vigilancia han sido instaladas desde 1995 dentro del programa de GAW por la OMM. Particularmente, en Chile, una de ellas es Cerro Tololo (TLL).

Altas (bajas) concentraciones de ozono se observan durante la tarde-noche (mañana). Su variabilidad mensual está relacionada a la quema de biomasa del hemisferio sur. El carbono-negro-equivalente muestra el mismo patrón diurno que ozono, altas (bajas) concentraciones en verano (invierno). Su variabilidad mensual está probablemente asociada a actividad humana en los valles de los alrededores. Exponentes de Angstrom muestran que TLL está influenciado por arena y, más hollín de carbono-negro que quema de biomasa.

Las parcelas de aire provienen de niveles superiores, sobre el océano y áreas contaminadas. Las primeras representan un intercambio entre estratósfera-tropósfera. Las segundas son producto de la brisa marina. Finalmente, las últimas representan el transporte local de los alrededores.

Dedicada a mi madre por todo su amor, apoyo, esfuerzo y comprensión durante el tiempo de estudio. Además, por permitirme estudiar lo que quise y darme la posibilidad de cumplir mis sueños...Patricio

AGRADECIMIENTOS

- ❖ A Dios, por darme una madre espectacular y por las personas que puso en mi camino.
- ❖ A mi madre y familia, por su confianza y apoyo en todos mis años de estudios y decisiones que he tomado.
- ❖ A la Universidad de Chile, por acogerme y darme un lugar donde realizar el presente trabajo.
- ❖ A los profesores, compañeros y amigos del programa de Magíster en Meteorología y Climatología por el incondicional apoyo y por los momentos inolvidables que hemos vivido.
- ❖ A los integrantes de la comisión, en especial a Nicolas Bukowiecki por estar siempre presente desde antes del inicio de la tesis.
- ❖ A mi profesor Guía Nicolás Huneus por su ayuda, disposición y buena voluntad durante todo el trabajo.
- ❖ Al centro de investigación CR2 por haber costeado el programa de magíster.
- ❖ A el proyecto CATCOS por brindarme la posibilidad de realizar una capacitación sobre el tema de este trabajo.
- ❖ Finalmente a todas las personas que se cruzaron en mi camino y que me dieron palabras de aliento y apoyo.

TABLA DE CONTENIDO

1.- Presentation and Background.....	1
1.1.- Introduction	1
1.2.- Goals	4
1.2.1.- Main Goal.....	4
1.2.2.- Secondary Goals.....	5
1.3.- Concepts	5
1.3.1.- Ozone	5
1.3.2.- Aerosols.....	5
1.3.3.- Optical Properties of aerosols	7
2.- Data Base and Methods.....	10
2.1.- Instruments and Data Base description	10
2.1.1.- Instruments	10
2.1.2.- Data Base	11
2.1.2.1.- Equivalent Black Carbon	12
2.1.2.2.- Angstrom exponent	12
2.2.- Basic Statistics	14
3.- Results	15
3.1.- Variability Analysis	15
3.1.1.- Ozone	15
3.1.3.- Equivalent Black Carbon	17
3.1.4.- Angstrom Exponents	21
3.2.- Case Study.....	24
4.- Conclusions	30
5.- Bibliography.....	32
Appendix A - List of abbreviations	37

ÍNDICE DE TABLAS

Table 1. Parameters which are used to aerosol amount and type.	8
--	---

ÍNDICE DE ILUSTRACIONES

Figure 1. Location of Cerro Tololo (30°S, 70°W, 2200 m.a.s.l.). The map to the upper-left shows altitude contours in meters for the intervals: <0, 0–50, 50–200, 200–500, 500–2000, 2000–3500, 3500–5000 and above 5000 m. (Gallardo, Carrasco, & Olivares, 2000). Bottom shows a cross-section at 30°S, red circle represents Cerro Tololo site, bottom (right) axes shows horizontal distance from coastline (altitude) in kilometers (meters).	2
Figure 2. Monthly averages of ozone at Cero Tololo. The observation period is between April 1996 until April 1998. Error bars indicate one standard deviation of the mean. Figure from Gallardo, Carrasco, & Olivares (2000).	3
Figure 3. The upper panels show composite time series of ozone anomalies (solid curve) and water vapor pressure anomalies (dashed curve) for (a) W and (b) D cases relative to average values for the selected episode. The lower panels show the 12h-window running mean omega velocity (from NCEP/ NCAR reanalysis) composites for (c) W and (d) D cases at two different vertical levels over a grid point at 30°S and 70°W. Recall that negative values indicate upward motion. Dashed vertical lines indicate the initial increase in ozone. The solid curve represents 500-hPa, and the dashed curve represents 200-hPa. Figure from Rondanelli, Gallardo, & Garreaud (2002).	4
Figure 4. Scheme how to calculate absorption coefficient after introducing corrections in the attenuation coefficient obtained from Lambert-Beer Law (by Budi Satria, GAW Bukit Kototabang Station).	8
Figure 5. Scatter plot of AAE vs. organic fraction of submicron non-refractory aerosol mass, color coded by scattering Angstrom exponent. Results are from in situ measurements of aerosols by absorption photometer, nephelometer, and aerosol mass spectrometer on the C-130 mostly over Central Mexico during MILAGRO in March 2006 (Shinozuka Y. , Clarke, Howell, & al., 2008; DeCarlo, et al., 2008; Shinozuka Y. , et al., 2009). AAE and SAE are for total particles observed behind the aircraft inlet. (i.e., not submicron aerosol). Figure from Russel, et al. (2010).	9
Figure 6. Fixed panoramic picture of Cerro Tololo (by Nicolas Bukowiecki), dotted yellow circle represents Aerosol-ozone station.	11
Figure 7. Aerosol-ozone station at Cerro Tololo (by Nicolas Bukowiecki).	11
Figure 8. Hourly ozone distribution at TLL during 2013-2015.	15
Figure 9. Boxplot, diurnal cycle of hourly ozone concentrations [ppbv] at TLL during 2013-2015. Top and bottom of boxes mean percentile 25 and 75 (p25 & p75, respectively), red line in box represents median value for each hour, extreme of top and bottom dashed lines represent (2.5*p25 - 1.5*p75) and (2.5*p75 - 1.5*p25), and red marker are taken as outliers.	16
Figure 10. Daily ozone concentrations [ppbv] at TLL during 2013-2015.	16
Figure 11. Top: Time series of monthly ozone concentrations [ppbv] at TLL during 2013-2015. Red markers represent average for each month, top and bottom black bars are one standard deviation each. Bottom: amount of days in each month that are used to calculate monthly averages and standard deviations.	17
Figure 12. Boxplot, monthly cycle of daily ozone concentrations at TLL during 2013-2015. Top and bottom of boxes mean percentile 25 and 75 (p25 & p75, respectively), red line in box represents median value for each month, black markers mean average value of each month,	

extreme of top and bottom dashed lines represent $(2.5 \cdot p_{25} - 1.5 \cdot p_{75})$ and $(2.5 \cdot p_{75} - 1.5 \cdot p_{25})$, and red marker are taken as outliers.17

Figure 13. Hourly distribution of eBC concentrations at Cerro Tololo during 2013-2015.18

Figure 14. Daily series of eBC at TLL during 2013-2015.19

Figure 15. Boxplot, diurnal cycle of hourly eBC concentrations at TLL during 2013-2015. Top and bottom of boxes mean percentile 25 and 75 (p_{25} & p_{75} , respectively), red line in box represents median value for each hour, extreme of top and bottom dashed lines represent $(2.5 \cdot p_{25} - 1.5 \cdot p_{75})$ and $(2.5 \cdot p_{75} - 1.5 \cdot p_{25})$, and red marker are taken as outliers.19

Figure 16. Top: monthly series of eBC concentrations at TLL during 2013-2015. Red markers represent average for each month, top and bottom black bars are one standard deviation each. Bottom: amount of daily averages in each month that are used to calculate monthly standard deviations and averages.20

Figure 17. Boxplot, monthly cycle of daily eBC concentrations at TLL during 2013-2015. Top and bottom of boxes mean percentile 25 and 75 (p_{25} & p_{75} , respectively), red line in box represents median value of each month, black markers mean average value of each month, extreme of top and bottom dashed lines represent $(2.5 \cdot p_{25} - 1.5 \cdot p_{75})$ and $(2.5 \cdot p_{75} - 1.5 \cdot p_{25})$, and red marker are taken as outliers.20

Figure 18. Hourly distribution at Cerro Tololo during 2013-2015. Top for AAE, middle SAE and bottom SSAAE.21

Figure 19. Boxplot, diurnal cycle of hourly Angstrom exponents at TLL during 2013-2015. Left for AAE, middle SAE and right SSAAE. Top and bottom of boxes mean percentile 25 and 75 (p_{25} & p_{75} , respectively), red line in box represents median value for each hour, extreme of top and bottom dashed lines represent $(2.5 \cdot p_{25} - 1.5 \cdot p_{75})$ and $(2.5 \cdot p_{75} - 1.5 \cdot p_{25})$, and red marker are taken as outliers.22

Figure 20. Time series of daily Angstrom Exponents at Cerro Tololo during 2013-2015. Top for AAE, middle SAE and bottom SSAAE. Black (yellow, B and C) zones represent BC (dust, A and D) episodes.23

Figure 21. Monthly series of Angstrom Exponents at Cerro Tololo during 2013-2015. Top for AAE, middle SAE and bottom SSAAE. Black (yellow, C) zones represent BC (dust, D) episodes.23

Figure 22. Monthly cycle at TLL for Dust Events: left represents boxplot of daily concentrations of ozone, middle boxplot of daily concentrations of eBC, and right monthly values of scattering coefficients.24

Figure 23. Monthly cycle at TLL for NO Dust Events: left represents boxplot of daily concentrations of ozone, middle boxplot of daily concentrations of eBC, and right monthly values of scattering coefficients.25

Figure 24. Dust case, 07/Mar/2014. Aerosol optical properties: top AAE, middle SAE, and bottom SSAAE. Yellow zone represents DU event.26

Figure 25. Dust case, 07/Mar/2014. Top ozone, bottom eBC, and bottom scattering coefficient. Yellow zone represents DU event.26

Figure 26. Dust case, 04/Nov/2014. Aerosol optical properties: top AAE, middle SAE, and bottom SSAAE. Yellow zone represents DU event.27

Figure 27. Dust case, 04/Nov/2014. Top ozone, bottom eBC, and bottom scattering coefficient. Yellow zone represents DU event.27

Figure 28. NO dust case, 24/Dec/2013. Aerosol optical properties: top AAE, middle SAE, and bottom SSAAE. Yellow zone represents ND event.28

Figure 29. NO dust case, 24/Dec/2013. Top ozone, bottom eBC, and bottom scattering coefficient. Yellow zone represents ND event.28

Figure 30. NO dust case, 05/May/2015. Aerosol optical properties: top AAE, middle SAE, and bottom SSAAE. Yellow zone represents ND event.29

Figure 31. NO dust case, 05/May/2015. Top ozone, bottom eBC, and bottom scattering coefficient. Yellow zone represents ND event.29

1.- Presentation and Background

1.1.- Introduction

Aerosols are particles (liquid or solid phase) suspended in the air (Seinfeld & Pandis, 2012) which affect the Earth in different ways. For example, they absorb and scatter the radiation inside the atmosphere which modifies the planetary energy balance (Penner, et al., 2001; NASA, 2010). Similarly, they also impact solar radiation by modifying cloud properties (albedo and lifetime; Penner, et al., 2001; NASA, 2010). In addition, aerosols are deposited on marine-ice, snow and glaciers surfaces, which change their energy balance by increasing sunlight absorption warming them up and enhancing the melting of snow and ice cover, i.e., (Stier, Seinfeld, Kinne, Boucher, & Boucher, 2007).

Ozone (O₃- gas phase) is vital to human well-being. On one hand, most ozone resides high up in the atmosphere (stratosphere) and it contains about 90% of all the ozone in the atmosphere absorbing the harmful sun-ultraviolet radiation which acts as an effective greenhouse gas playing an important role in the stratospheric thermal structure (Holton & Hakim, 2013). On the other hand, the less ozone resides at the surface (or lower atmosphere) helping to remove pollutants from the troposphere (Crutzen, 1995). However, excess ozone at Earth's surface, that is formed from pollutants, can be harmful to humans, plants, and animals (Brunekreff & Holgate, 2002; Organization & Europe, 2006).

The impact of aerosols on the radiative balance is partly determined by their optical properties, which illustrate the absorption and scattering capacity of the atmosphere. The variability of these properties has been documented in many places of the world (Holben, et al., 2001; Chung, Ramanathan, Kim, & Podgorny, 2005). Because the impact of the aerosols varies regionally and the global impact is not easily quantified, it is necessary to have a look of aerosol optical properties in several places of world. Furthermore, increasing O₃ concentrations have been observed in the troposphere due to anthropogenic activities linked to hydrocarbons and nitrogen oxides emissions (Tilmes S. , et al., 2011; Tilmes S. , et al., 2012; Ziemke, et al., 2011). Measurements of O₃ at remote places are key to assess the impact of the anthropogenic activities on atmospheric composition (WMO/GAW, 2011). In view of this, since mid 90s multiple watching stations have been installed as part of Global Atmospheric Watch Program (GAW) by the World Meteorological Organization (WMO). Particularly, in Chile, one of them corresponds to Cerro Tololo (TLL) which is managed by the Chilean Weather Office (DMC, from Spanish Dirección Meteorológica de Chile) in cooperation with the Interamerican Southern Astronomical Observatory.

TLL is at 30°S, 70°W and 2.200 m.a.s.l. close to the city of La Serena located near the western coast of South America in a region where the Andes mountains have an average altitude of 4000 m and a width of 200 km (figure 1). This region is placed in a north-south transition zone between the arid conditions of the Atacama Desert and the Mediterranean climate of Central Chile (Miller, 1976). It is characterized by the influence of the subsiding branch of the Hadley cell and the South Pacific High which both produce a permanent subsidence over the area being rarely interrupted by synoptical disturbances linked to bad weather conditions during winter. Precipitation at TLL (less than 100 mm per year) takes place in winter during a few episodes (fronts and cutoff lows) whose frequency and intensity have a large interannual variability (Rutllant & Fuenzalida, 1991; Pizarro & Montecinos, 2000). Gallardo et al. (2000) describe the

vertical development of clouds at the coast of TLL which is capped by the subsidence at about 1500 m.a.s.l. and the boundary layer contained below 850 hPa indicating that coastal air parcels are not able to reach TLL because its location must be above the thermal inversion layer. In this way, TLL is known because its location is in the free atmosphere affected by a subsidence regime that brings clear sky conditions.

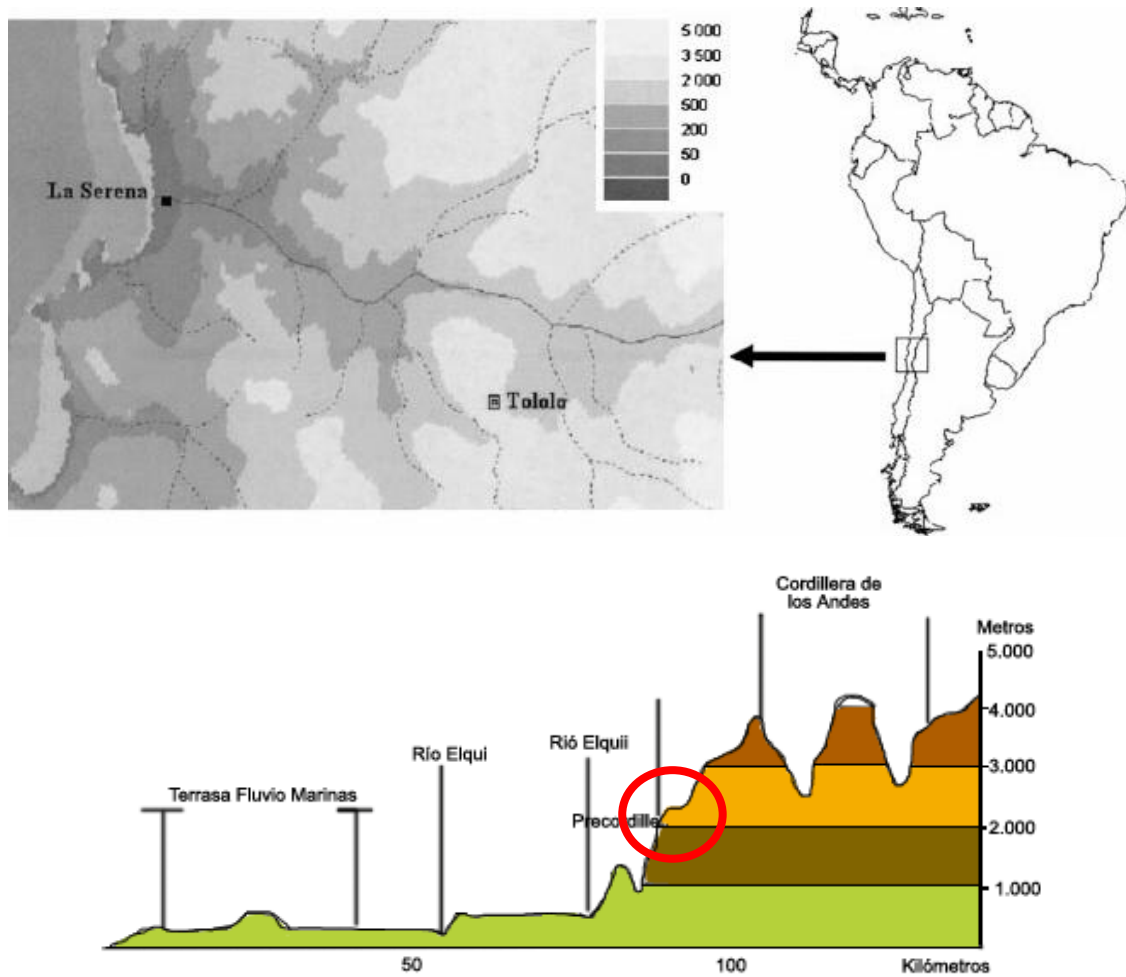


Figure 1. Location of Cerro Tololo (30°S, 70°W, 2200 m.a.s.l.). Top shows altitude contours in meters for the intervals: <0, 0–50, 50–200, 200–500, 500–2000, 2000–3500, 3500–5000 and above 5000 m. Figure(Gallardo, Carrasco, & Olivares, 2000). Bottom shows a cross-section at 30°S, red circle represents Cerro Tololo site, bottom (right) axes shows horizontal distance from coastline (altitude) in kilometers (meters).

The first work about Cerro Tololo is the ozone data analysis which is done for two years since April 1996 (Gallardo et al, 2000). For this period the data show a seasonal variation with maximum mixing ratios in late winter and spring and minimum mixing ratios in late summer and early fall (figure 2). These variations are most likely associated with the large-scale subsidence of the Hadley circulation and the location of the subtropical jet stream (STJ). Also, there is a diurnal variation that is probably partly associated with a mountain wind flow which is strongest in late spring and summer months. Few years later Kalthoff, et al. (2002) study the atmospheric flow conditions at Cerro Tololo. Different wind regimes are distinguished; above 4000 m.a.s.l. large-scale westerlies prevail, while northerly winds are observed in a band along the coastline between

2000-4000 m.a.s.l.. This wind regime results from the westerly winds being blocked by the Andes and forced to flow parallel to it. Moreover, seasonally varying, thermally induced valley winds and a sea breeze develop below the northerly wind regime, potentially reaching the Cerro Tololo site.

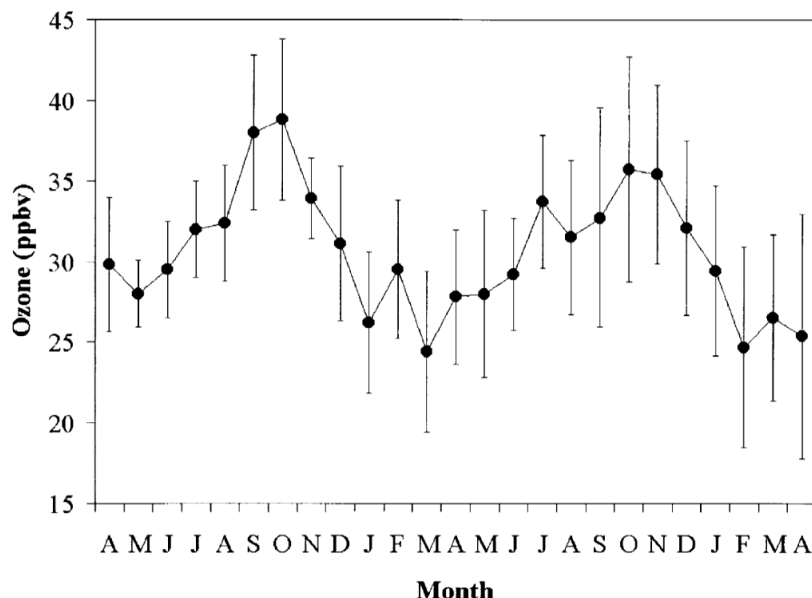


Figure 2. Monthly averages of ozone at Cerro Tololo. The observation period is between April 1996 until April 1998. Error bars indicate one standard deviation of the mean. Figure from Gallardo, Carrasco, & Olivares (2000).

Rondanelli et al. (2002) analyze the rapid changes in surface ozone mixing ratios at the Cerro Tololo station over the period 1996–2000. Local circulations and in situ photochemical processes cannot account for the sudden changes in ozone. Synoptic patterns associated with sudden changes in ozone concentration are separated into 2 cases (Dry and Wet; figure 3). In both cases, D and W, stratospheric air appears to be advected from polar latitudes to mid-latitudes and subtropical latitudes during the development of cutoff lows and deep troughs (Fuenzalida et al., 2005). For D cases the stratospheric intrusion is mostly confined to mid-latitudes and to an oceanic area far from the site of study. W cases show a deep stratospheric intrusion reaching the lower troposphere in subtropical latitudes during the amplification and mature stages of a cutoff low. Those intrusions are produced by synoptic and meso-scale mechanism that force a vertical interchange troposphere-stratosphere, which partially controls the ozone concentration (Holben, et al., 2001; Škerlak, Sprenger, & Wernli, 2014). The mechanism might be enhanced by lower-scale circulations, for example see-valley-mountain circulation (Mahrer & Pielke, 1977) that produces a higher variability in near-surface ozone concentrations.

In view of the important role of aerosols and ozone to human well-being, climate, and to the evaluation of the impacts of the anthropogenic activities, the purpose of this work is to illustrate a part of the subtropics free-atmosphere composition and its temporal variability during 2013-2015. Additionally, it is the first aerosol analysis done at TLL.

This work is organized as follows; the main and secondary goals are shown in section 1.2; important concepts such as equivalent black carbon, aerosols, ozone, optical properties, are

introduced in section 1.3. In the second chapter the instruments and database are presented and the methods used for the statistical analysis as well the variability analysis for the entire period and specific events are described. The results and the discussion are presented in the third chapter. Finally, the conclusions are presented in the fourth chapter.

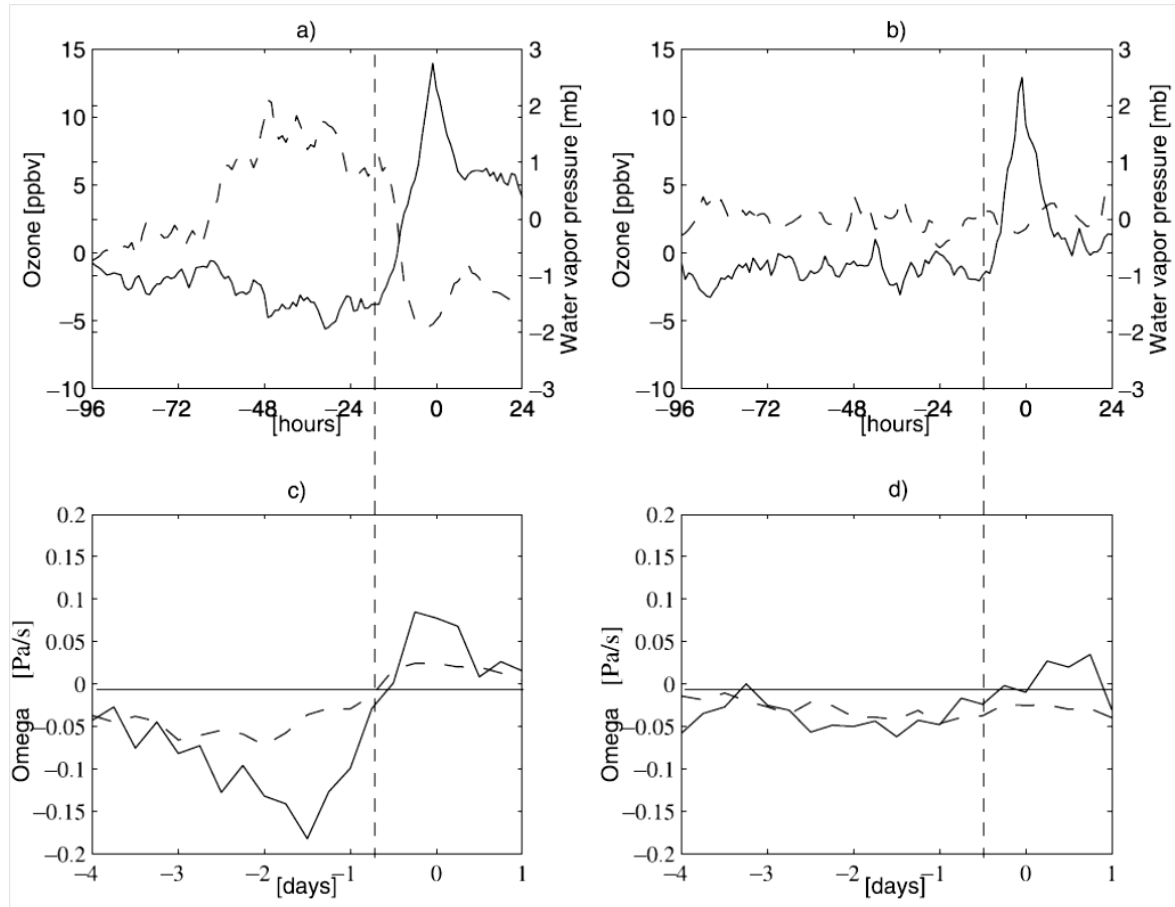


Figure 3. The upper panels show composite time series of ozone anomalies (solid curve) and water vapor pressure anomalies (dashed curve) for (a) W and (b) D cases relative to average values for the selected episode. The lower panels show the 12h-window running mean omega velocity (from NCEP/ NCAR reanalysis) composites for (c) W and (d) D cases at two different vertical levels over a grid point at 30°S and 70°W. Recall that negative values indicate upward motion. Dashed vertical lines indicate the initial increase in ozone. The solid curve represents 500-hPa, and the dashed curve represents 200-hPa. Figure from Rondanelli, Gallardo, & Garreaud (2002).

1.2.- Goals

1.2.1.- Main Goal

Analyze the temporal variability of ozone, equivalent black carbon and aerosol optical properties at Cerro Tololo (30°S, 70°W, 2.200 m.a.s.l.) during 2013-2015 and examine specific events.

1.2.2.- Secondary Goals

- Establish data series of ozone, equivalent black carbon and aerosol optical properties.
- Characterize the diurnal, seasonal and interannual variability of ozone, equivalent black carbon and aerosol optical properties.
- Identify events according to the dust index and explain variability patterns of the other variables.
- In-depth analysis of the variability of ozone, equivalent black carbon and angstrom exponents for four of the previous identified events

1.3.- Concepts

This work focuses in four important elements (namely ozone, black carbon, aerosols, and optical properties of aerosols) whose definitions are explained in the following sections.

1.3.1.- Ozone

Ozone (O₃) is a natural gas whose molecules are formed by 3 oxygen atoms. It is found in two different atmospheric layers: the lowest layer of the troposphere near the surface and in the stratosphere. In the lowest layer the ozone plays a role as a pollutant usually called "photochemical smog" or "bad ozone", it is considered unhealthy for the livings being (humans, vegetation and other animals) (Brunekreff & Holgate, 2002; Organization & Europe, 2006) and it determines the oxidative capacity of the troposphere (Crutzen, 1995). On the other hand, in the stratosphere it plays a role as a UV-filter protecting the life in the Earth and also acts as an effective greenhouse gas participating in the stratospheric thermal structure (Holton & Hakim, 2013).

1.3.2.- Aerosols

Aerosols, particles suspended in a gas, can be separated as primary aerosols when they are emitted as such into the atmosphere and secondary aerosols when they are formed in the atmosphere by gaseous precursors. Their sources are several but are grouped into natural (e.g. desert dust, volcano plumes, sea salt, pollen) and anthropic (e.g. burning wood, fossil fuel, industrial processes) source. The aerosols can be described based on their size, whose range is between 0.001 and 100 μm (Finlayson-Pitts & Pitts Jr., 1999; Seinfeld & Pandis, 2012). Several elements can be part of the aerosol composition, e.g., water (liquid and solid phase), carbon, minerals, dust, salt, microorganisms, etc. Depending on the aerosol composition, particles air-distribution and environmental humidity, i.e. on their hygroscopicity, the aerosols may absorb water vapor and increase their size (Petters & Kreidenweis, 2007). Because of the addition of humidity, the aerosol phase can be forced to change to liquid and depending the temperature to solid again, the understand of these processes are very important in the cloud and the climate research (Haywood & Boucher, 2000)

Aerosols cannot only influence climate through their direct interaction with solar radiation (e.g. scattering and absorbing light and changing Earth's reflectivity), but they can also alter the

climate through their impact on cloud optical and physical properties. On a global scale, these aerosol “indirect effects” typically work in opposition to greenhouse gases and cause cooling. Aerosols play a critical role in the formation process of clouds. In fact, most clouds owe their existence to aerosols that serve as the tiny “seeds” called cloud condensation nuclei (Petters & Kreidenweis, 2007; NASA, 2010).

Short-term and long-term exposures to aerosols affect plants (Rai, 2016) and human being (Brook, Brook, & Rajagopalan, 2003). Particularly, fine particles with size below 2.5 μm (referred to as PM_{2.5}) are associated with a broad range of human health impacts, including respiratory and cardiovascular effects, as well as premature death (Pope III, et al., 1995; Pope III, et al., 2002; Lei, Hwang, Chan, Lee, & Cheng, 2005; Kennedy, 2007; Proietti, R  sli, Frey, & Latzin, 2013). PM_{2.5} exposure, both ambient and indoor, is estimated to result in millions of premature deaths worldwide (Sasser, et al., 2012).

Carbonaceous aerosol is one of the aerosol species that is receiving currently increasing attention due to its impacts on the Earth's energy balance (Penner, et al., 2001; NASA, 2010; Bond, et al., 2013) A fraction of the carbonaceous aerosol, known as black carbon (BC), whose size is mostly measured between 1 and 10 μm , is a distinct type of carbonaceous material that is formed primarily in flames. It is directly emitted to the atmosphere by the combustion of fossil fuel and biomass, and characterized by its strong absorption of visible light and its resistance to chemical transformation (Ogren & Charlson, 1983; Goldberg, 1986; Bond, et al., 2013). As mentioned before, 3 important BC effects on climate are summarized following (Sasser, et al., 2012), which also are associated with all ambient particles, but not GHGs:

- Direct effect: BC absorbs both incoming and outgoing radiation at all wavelengths, which contributes to warming of the atmosphere and dimming at the surface. In contrast, GHGs mainly trap outgoing infrared radiation from the Earth’s surface.
- Snow/ice albedo effect: BC deposited on snow and ice darkens the surface and decreases reflectivity (albedo), thereby increasing absorption and accelerating melting. GHGs do not directly affect the Earth’s albedo.
- Other effects: BC also alters the properties and distribution of clouds, affecting cloud reflectivity and lifetime (“indirect effects”), stability (“semi-direct effect”), and precipitation.

These properties give it relevance in various research fields related to climate change, air chemistry, air quality, paleoclimatology, etc (e.g., Yang, Xu, Cao, Zender, & Wang, 2015; Ching, Riemer, & West, 2016). The BC is also included in the Strategic Plan of the Global Atmosphere Watch program (GAW) of the World Meteorological Organization (WMO) (M  ller, et al., 2007). It becomes one of the key targets for current research on the aerosol impact on climate and related mitigation strategies (Stocker, et al., 2013; Paris 2015 UN Climate Change Conference COP21 - CMP11). Emission control policies of the light-absorbing carbonaceous (LAC) aerosols, referred to as a short-lived climate forcer, are contemplated as a near-term mitigation strategy for the climate impacts of anthropogenic emissions (WMO/GAW (2011)).

They are many different ways to quantify the amount of BC (Bond, et al., 2013; Petzold, et al., 2013) and one of them, called equivalent black carbon (eBC), is the key of this work. EBC

is referred to the mass concentration of BC and is obtained by photometric absorption measurements and is calculated by the equation 2 (see section 2.1.2.) adding a special coefficient (MAC(λ), mass absorption cross section, equation 3 in section 2.1.2.), which according to the studied area varies significantly in time and space depending upon source emissions, transformation during transport, etc. The application of this coefficient, i.e., conversion, assumes that eBC is the only light-absorbing particulate species present and contributions from non-carbonaceous light-absorbing aerosol components like mineral dust or non black carbon are neglected (Andreae & Gelencsér, 2006; Petzold, et al., 2009; Petzold, et al., 2011). The light absorption per mass is described using the term “mass absorption cross-section” (MAC) and indicates that the absorption cross section is referenced or normalized to the mass of the particle.

1.3.3.- Optical Properties of aerosols

The capacity of aerosols to absorb and scatter light is determined by their aerosol optical properties which in turn determine the Earth' energy balance. These properties are defined as the interaction between light and particles, in other words, when light collides with the particles (e.g. extinction, absorption and scattering of light). They are quantified by several numerical methods depending on the type of the measurements (e.g., in situ: Herrmann, et al., 2014 ; remote sensing: Lenoble, Remer, & Tanré, 2013). Moreover, the science community uses the terms “Aerosol amount” (proportional to aerosol loading, amount) and "Aerosol type" (composition, shape, size) properties to be able to clearly describe the particles (table 1).

Some properties are explained by three aerosol coefficients that are derived from the Lambert-Beer Law (see equation 1, and scheme for one of the coefficients in the figure 4), namely: aerosol extinction coefficient $\sigma_{\text{ext}}(\lambda)$, aerosol absorption coefficient ($\sigma_{\text{abs}}(\lambda)$) and the aerosol scattering coefficient ($\sigma_{\text{scat}}(\lambda)$). $\sigma_{\text{ext}}(\lambda)$ is the sum of $\sigma_{\text{abs}}(\lambda)$ and $\sigma_{\text{scat}}(\lambda)$, which are used to quantify the absorbing and scattering effects of the measured aerosol and both depend on the light-wavelength emitted by the instrument. $\sigma_{\text{abs}}(\lambda)$ is defined as the light-absorbing part of the light extinction. Similarly, $\sigma_{\text{scat}}(\lambda)$ is defined as the light-scattering part of the light extinction. Otherwise, there is another property called single scattering albedo (SSA) that is defined as the fraction of aerosol scattering to aerosol extinction (equation 6, see section 2.1.2.) and also depends on the light-wavelength.

These three aerosol coefficients (extinction, scattering and absorption) and SSA are not enough to characterize the aerosol optical properties and it is necessary to calculate other parameters which give more information about the particles. The so called Angstrom exponents describe the power-law wavelength dependence of the above coefficients and are defined to be the respective power law exponent. The Angstrom exponents are used to characterize the type and size of aerosols. Three Angstrom exponents are used in this work that are derived from absorption and scattering coefficients (equations 4-7). Absorption Angstrom exponent (AAE) values close to or between 1.0 and 1.5 correspond to pure BC (figure 5) and large AAE values indicate absorbing aerosols from biomass/biofuel burning (Kirchstetter, Novakov, & Hobbs, 2004; Schnaiter, et al., 2006; Russel, et al., 2010; Kim, et al., 2012; Petzold, et al., 2013). Additional, the scattering Angstrom exponent (SAE) relates inversely to particle size, with values close to zero generally represents dust due to the large size (figure 5). Finally, the mineral dust particles can be differentiated from other coarse mode particles like sea salt by their characteristic spectral behavior of single scattering albedo Angstrom Exponent (SSAAE) in the optical range of $\lambda = 450\text{-}700$ nm, known as Dust-Index (Coen, et al., 2004). Dust events show significantly

negative values (below 0) of SSAAE, which is mainly caused by a large increase of coarse mode particles with a reddish color (Saharan Dust) (Coen, et al., 2004).

$$I = I_0 * e^{-\sigma_{abs} * x}$$

Equation 1

I_0 : the intensity of the incoming light

I : the remaining light intensity after passing through a medium with thickness x

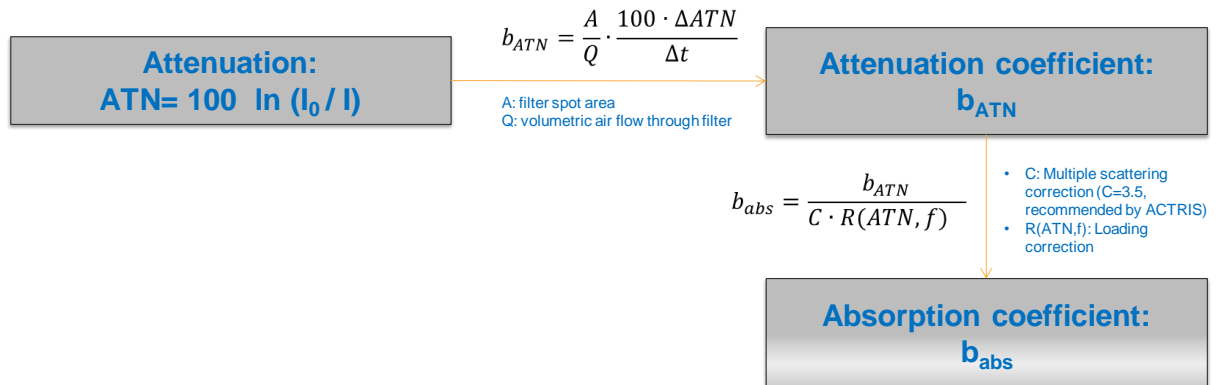


Figure 4. Scheme how to calculate absorption coefficient after introducing corrections in the attenuation coefficient obtained from Lambert-Beer Law (by Budi Satria, GAW Bukit Kototabang Station).

Table 1. Parameters which are used to determine aerosol amount and type.

Aerosol Amount	Aerosol Type
eBC	SSA
$\sigma_{abs}(\lambda)$	AAE
$\sigma_{scat}(\lambda)$	SAE
	SSAAE

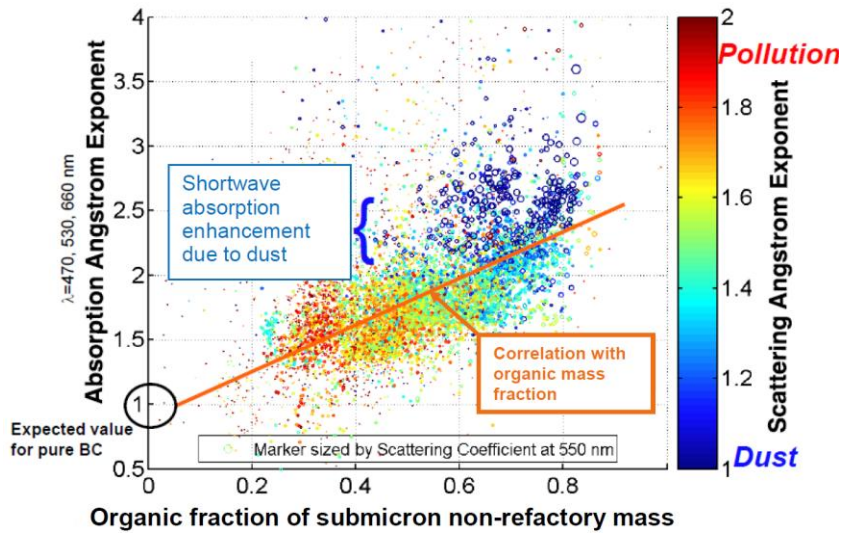


Figure 5. Scatter plot of AAE vs. organic fraction of submicron non-refractory aerosol mass, color coded by scattering Angstrom exponent. Results are from in situ measurements of aerosols by absorption photometer, nephelometer, and aerosol mass spectrometer on the C-130 mostly over Central Mexico during MILAGRO in March 2006 (Shinozuka Y. , Clarke, Howell, & al., 2008; DeCarlo, et al., 2008; Shinozuka Y. , et al., 2009). AAE and SAE are for total particles observed behind the aircraft inlet. (i.e., not submicron aerosol). Figure from Russel, et al. (2010).

2.- Data Base and Methods

In this chapter the data base including its measurements is described and the methods of optical properties interpretations, Equivalent Black Carbon calculation, basic statistic and further analysis are defined.

2.1.- Instruments and Data Base description

The instruments characteristics, their calibrations and the data base description is shown below.

2.1.1.- Instruments

In 2013, within the framework of the Swiss CATCOS Project, TLL is equipped with a new ozone photometer and a set of meteorological sensors covering different variables (temperature, wind, pressure, solar radiation and humidity). Ozone is measured by UV absorption with a Thermo Environmental Instruments Inc. TECO 49c analyzer. The station is equipped with an external ozonator which allows producing defined levels of ozone to conduct performance checks. Measurements are done continuously and data are recorded on a Campbell Scientific 21X data logger as 15-minute averages. Zero and span checks on multiple levels are done twice weekly and once monthly, respectively. Regularly, the operator inspects the recorded data for obvious anomalies. The TECO 49-003 analyzer measures the UV light absorption in the Hartley band (220-310 nm.) where ozone is a strong absorber. The optical bench is a dual cell device which is connected to a mercury lamp (245 nm) as light source. Alternately, one cell is flushed with ozone-free air while the other is simultaneously flushed with sample air. This allows a correction for changes in light intensity and potential interfering species. The TECO 49-003 has a sensitivity of ± 1 ppb and a precision of 2 ppb. The response time is on the order of 20 seconds to reach 95% of the new signal.

An Aethalometer and a Nephelometer are used to analyze the optical properties of aerosols and to estimate the equivalent black carbon. First, the Aethalometer, model AE31 manufactured by Magee Scientific, Berkeley, California, USA (Magee Sci. Inc.), is a multi-wavelength aerosol light-absorption photometer that measures the concentration of optically absorbing aerosol particles in real time. It operates at wavelengths of 370 nm, 470 nm, 520 nm, 590 nm, 660 nm, 880 nm, and 990 nm and is used to estimate the Equivalent Black Carbon by direct-internal instrumental algorithms or later calculations applying some corrections regarding to the zone where it is measured. Every two weeks filters and flow are checked. The 2-min average noise level of the Aethalometer is 0.7 Mm^{-1} , a detailed uncertainty assessment was performed by Müller, et al. (2007).

The Aurora 3000 Integrating Nephelometer measures, continuously and in real-time, light scattering in a sample of ambient air due to the presence of particles using an led light as source at three wavelengths: 525 nm. (green), 450 nm. (blue) and 635 nm. (red). This provides a wide and in-depth analysis of the interaction between light and aerosols. It includes backscatter measurements that allow both standard integrating measurements of $9\text{-}170^\circ$ and also the back scatter $90\text{-}170^\circ$. The measured values are adjusted automatically and in real-time by on-board temperature and pressure sensors. Zero and span checks and a full calibration with CO_2 are done

every thirty six hours and every three months, respectively. The Nephelometer has a detection limit of 0.3 Mm^{-1} and its measurements are 5 minutes averages.

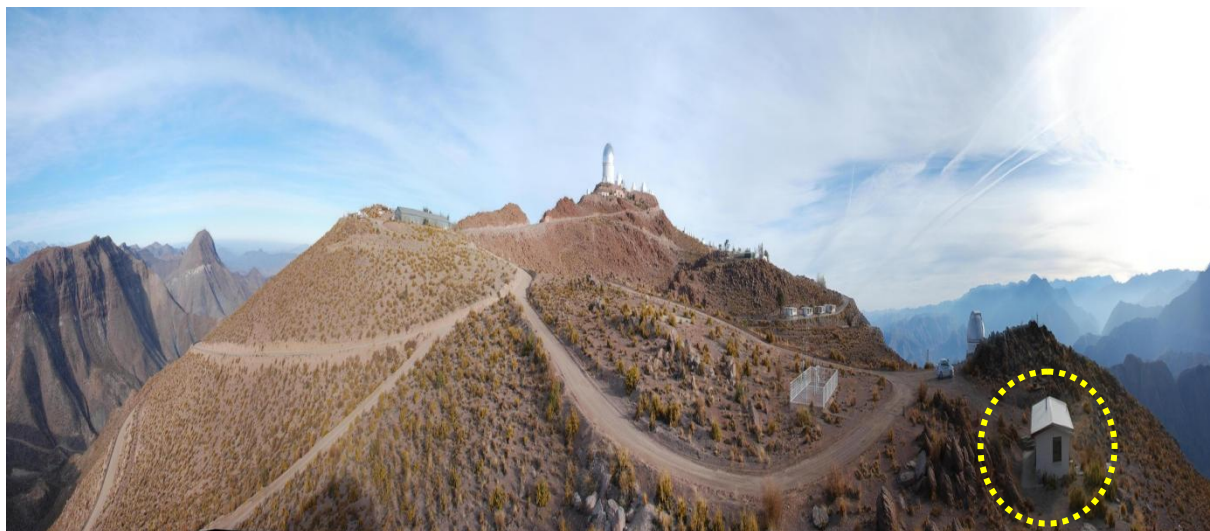


Figure 6. Fixed panoramic picture of Cerro Tololo (by Nicolas Bukowiecki), dotted yellow circle represents Aerosol-ozone station.



Figure 7. Aerosol-ozone station at Cerro Tololo (by Nicolas Bukowiecki)

2.1.2.- Data Base

The data base is set at UTC time for this work and the local time is used and defined as UTC-4 hours. Data are split into two-groups: ozone and aerosols. In both, the time resolution is hourly averages for the period from January 2013 till December 2015. The variables for the first group are surface-ozone concentration while for the second group they are scatter coefficient, absorption coefficient, eBC concentration and Angstrom Exponents. The equations of these variables are explained in the next sections.

2.1.2.1.- Equivalent Black Carbon

The eBC is computed based on the absorption coefficient and MAC at 880 nm (equation 2) because theoretical considerations and laboratory experiments show that, even with the same instrumental setup, light attenuation varies considerably as a function of the LAC content of the aerosol. These problems increase toward lower wavelengths, and therefore white light at an effective wavelength of 880 nm, used by the Aethalometer, is likely to be less affected.

Literature provides values of MAC for arid zones at 637 nm and the corresponding value at the wavelength of interest must be computed following equation 3. A commonly cited value for MAC ($MAC(\lambda_b)$) is $10 \text{ m}^2/\text{g}$ at a wavelength of 637 nm (Donoian & Medalia, 1967; Bond & Bergstrom, 2006; Knox, et al., 2009). Measurements uncorrected for enhancement by filter media also provide values of $10 \text{ m}^2/\text{g}$ (Horvath, 1993b; Petzold, Kopp, & Niessner, 1997; Bond, Anderson, & Campbell, Calibration and intercomparison of filter-based measurements of visible light absorption by aerosols, 1999; Fuller, Malm, & Kreidenweis, 1999). A large body of literature suggests that some ambient aerosol have mass absorption cross sections greater than $7.5 \text{ m}^2/\text{g}$ at 637 nm (see, e.g., Bond & Bergstrom, 2006).

The equation 2 is resolved using 880 nm as wavelength in the absorption coefficient and MAC coefficient.

$$eBC = \frac{\text{Absorption coefficient } (\lambda_a)}{MAC(\lambda_a)} \left[\frac{ng}{m^3} \right] \quad \text{Equation 2}$$

$$MAC(\lambda_a) = \left(\frac{\lambda_b}{\lambda_a} \right) * MAC(\lambda_b) \quad \text{Equation 3}$$

, by fixed Angstrom exponent = 1

λ_a : Wavelength for calculating eBC = 880 nm.

λ_b : Wavelength for calculating MAC using in eBC equation = 637 nm.

$MAC(\lambda_b)$: accorded MAC for arid zones at 637 nm. = $10 \text{ m}^2 \text{ g}^{-1}$.

2.1.2.2.- Angstrom exponent

The Absorption, Scattering and Single Albedo (i.e., Dust Index) Angstrom exponents are used to determinate the size and type (mineral or organic) of aerosols, and the presence of dust, respectively. These exponents are calculated from the coefficients described in the section 1.3.3.

Absorption angstrom exponent

$$AAE = - \frac{\ln \left(\frac{\sigma_{abs}(\lambda_1)}{\sigma_{abs}(\lambda_2)} \right)}{\ln \left(\frac{\lambda_1}{\lambda_2} \right)}$$

Equation 4

λ_1 : Lowest wavelength.

λ_2 : Highest wavelength.

σ_{abs} : Absorption coefficient depending on the wavelength.

Scattering Angstrom Exponent

$$SAE = - \frac{\ln \left(\frac{\sigma_{scat}(\lambda_1)}{\sigma_{scat}(\lambda_2)} \right)}{\ln \left(\frac{\lambda_1}{\lambda_2} \right)}$$

Equation 5

λ_1 : Lowest wavelength.

λ_2 : Highest wavelength.

σ_{scat} : Scattering coefficient depending on the wavelength.

Single Scattering Albedo Angstrom Exponent

$$\sigma_{SSA}(\lambda) = \frac{\sigma_{scat}(\lambda)}{\sigma_{ext}(\lambda)}$$

Equation 6

$\sigma_{ext}(\lambda)$: Extinction coefficient depending on the wavelength

$\sigma_{SSA}(\lambda)$: Single Scattering Albedo coefficient depending on the wavelength

$$SSAAE = - \frac{\ln \left(\frac{\sigma_{SSA}(\lambda_1)}{\sigma_{SSA}(\lambda_2)} \right)}{\ln \left(\frac{\lambda_1}{\lambda_2} \right)}$$

λ_1 : Lowest wavelength.
 λ_2 : Highest wavelength.

2.2.- Basic Statistics

The statistics used in this work are described as well as the method applied to process the data before being analyzed and assessed.

The hourly series of $\sigma_{abs}(\lambda)$ and $\sigma_{scat}(\lambda)$ present extreme values that are deleted by arbitrary criteria: for $\sigma_{abs}(\lambda)$ values over 20 Mm^{-1} and $\sigma_{scat}(\lambda)$ values over 100 Mm^{-1} .

All averages are calculated by the following method. The daily hourly values are grouped in 6 time slots; namely from 00 to 3 UTC, 4-7, 8-11-, 12-15, 16-19, and 20-23. The average for each group is calculated only if there are at least 3 values in each one. Afterwards, the daily average is calculated only if there are at least 5 groups averages in each day. Finally, the monthly averages are calculated only if there are at least 50% of the days of each month, except for some variables where is shown how many days are taken to calculate it.

The months are described in group of seasons. December, January and February correspond to summer; March, April and May to autumn; June, July and August to winter; and September, October and November correspond to spring.

The general distribution, diurnal and annual cycles, and variability of the data series are studied in this work using probability density functions (no fixed), boxplot and regular statistic (e.g., median, mean, standard deviation, etc). After that, the Dust and No-Dust events are identified by SSAAE (dust = SSAAE below zero and no-dust = above zero), and some of them are randomly selected to an in-depth analysis using the same method applied before.

3.- Results

In this chapter the results are shown in two groups: variability analysis (section 3.1) and study case (section 3.2).

3.1.- Variability Analysis

The temporal variability of Ozone, eBC and Angstrom Exponents are presented in this section. Hourly distribution, and daily and monthly series are analyzed and discussed.

3.1.1.- Ozone

During 2013-2015 ozone concentrations show an hourly-variability range between approximately 5-70 ppbv and a likely Gaussian distribution (Wilks, 2011). Maximal frequency is observed around 30 ppbv and at least 70% of the data is between 25-40 ppbv (figure 8). consistent with monthly values found in Gallardo et al. (2000; figure 2).

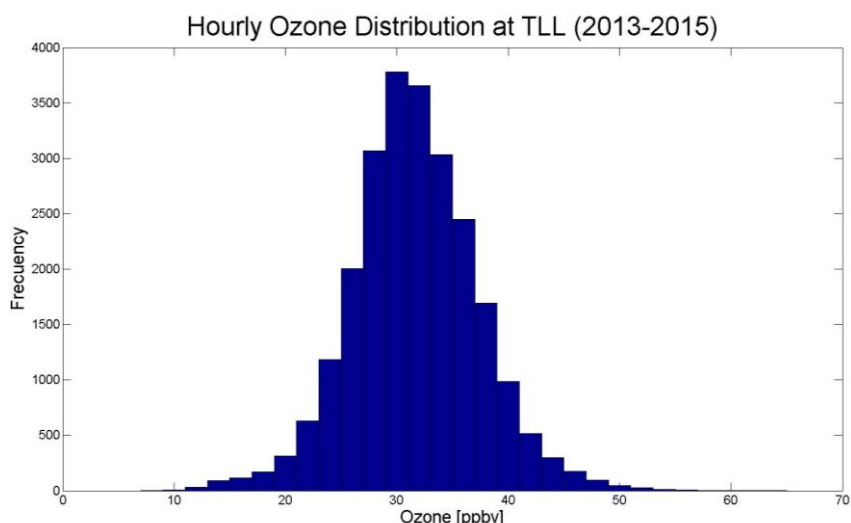


Figure 8. Hourly ozone distribution at TLL during 2013-2015.

Figure 9 shows the diurnal cycle of ozone concentrations for the same period, which has a low cycle-amplitude with maximal values during afternoon, evening and night, and minimum during morning. It also describes a median around 32 ppbv and the 50% of the data between 27-36 ppbv with extreme values, percentile 2.5 and 97.5, approximately around 17 and 47, respectively.

Monthly and daily averages show maximal ozone concentrations during spring and minimum summer (figures 10 and 11) similar as found in Gallardo et al. (2000) and Rondanelli et al. (2002). In addition, the monthly cycle for the same period shows maximal ozone concentrations in October and minimum in February with a difference of ca. 10 ppbv (figure 12). The maximal ozone concentration is probably associated to southern hemisphere biomass-burning as described in Gallardo et al. (2000) and Duncan et al. (2003).

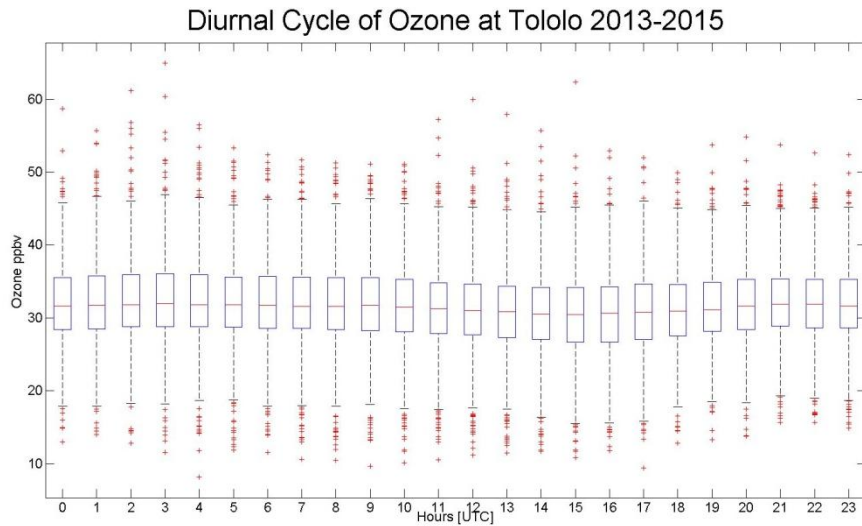


Figure 9. Boxplot, diurnal cycle of hourly ozone concentrations [ppbv] at TLL during 2013-2015. Top and bottom of boxes mean percentile 25 and 75 (p25 & p75, respectively), red line in box represents median value for each hour, extreme of top and bottom dashed lines represent $(2.5 \cdot p25 - 1.5 \cdot p75)$ and $(2.5 \cdot p75 - 1.5 \cdot p25)$, and red marker are taken as outliers.

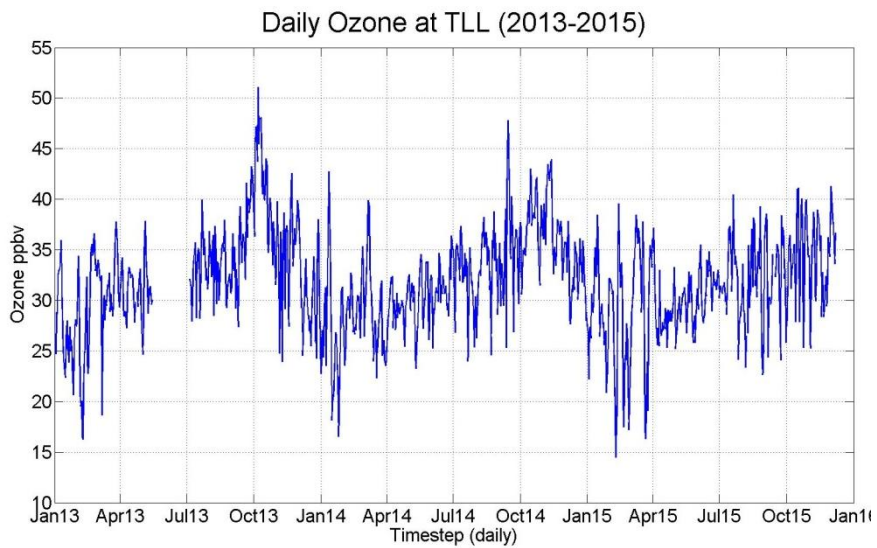


Figure 10. Daily ozone concentrations [ppbv] at TLL during 2013-2015.

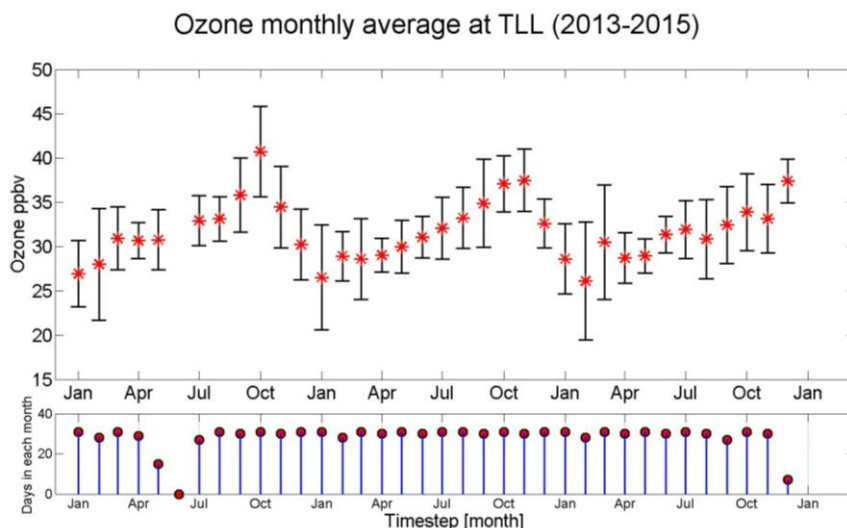


Figure 11. Top: Time series of monthly ozone concentrations [ppbv] at TLL during 2013-2015. Red markers represent average for each month, top and bottom black bars are one standard deviation each. Bottom: amount of days in each month that are used to calculate monthly averages and standard deviations.

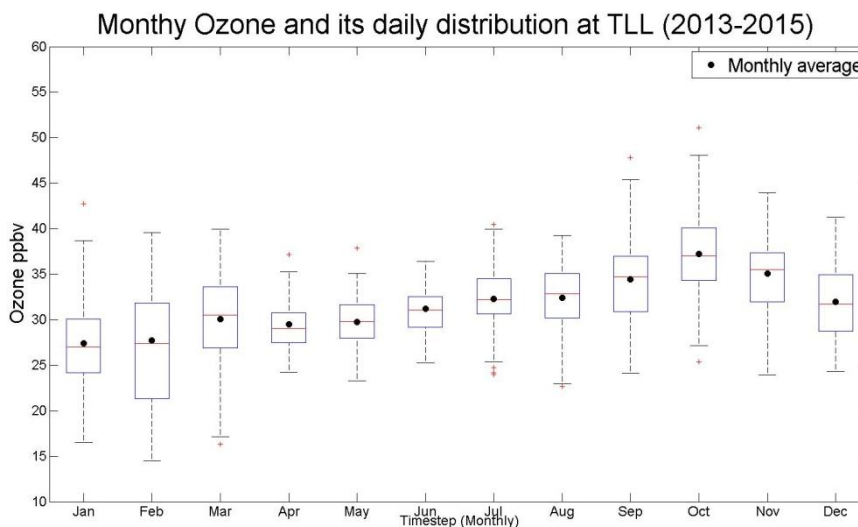


Figure 12. Boxplot, monthly cycle of daily ozone concentrations at TLL during 2013-2015. Top and bottom of boxes mean percentile 25 and 75 (p25 & p75, respectively), red line in box represents median value for each month, black markers mean average value of each month, extreme of top and bottom dashed lines represent $(2.5 \times p25 - 1.5 \times p75)$ and $(2.5 \times p75 - 1.5 \times p25)$, and red marker are taken as outliers.

3.1.3.- Equivalent Black Carbon

During 2013-2015 eBC shows an hourly-variability range between approximately $0-500 \text{ ngm}^{-3}$ and a likely Gamma distribution (Wilks, 2011). Maximal frequency is observed around 50 ngm^{-3} and at least 70% of the data is between $25-150 \text{ ngm}^{-3}$ (figure 13).

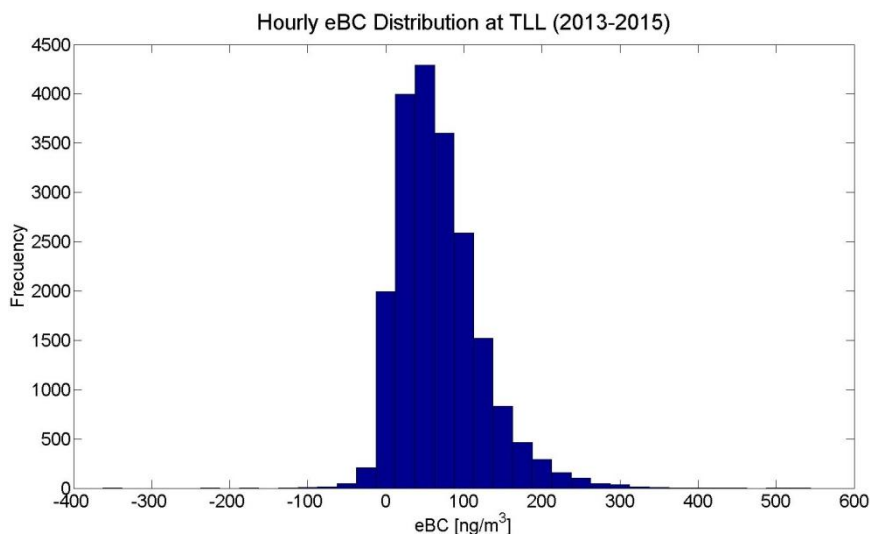


Figure 13. Hourly distribution of eBC concentrations at Cerro Tololo during 2013-2015.

Time series of daily eBC concentrations presents high daily amplitude throughout the period (figure 14), which can be modulated by daily changes in the synoptic-, meso- and local scale patterns. It also shows low daily eBC concentrations during winter likely linked to cleaner air masses, deposition due to rain or less human activity in the surrounding valleys. In contrast, high daily values around 250 ngm^{-3} are observed during summer and early autumn.

On one hand, these high values can be related to more human activities in the surrounding valleys because there is school vacation during the same period (summer) which may mean several barbecues in the surrounding areas, and these valley air-parcels can reach TLL because of regular valley-mountain circulations described by Gallardo et al. (2000), Kalthoff, et al. (2002) and Montecinos et al. (2016). On the other hand, these high values of eBC can be also linked to forest fires that occur in the same region or surrounding it during summer, e.g. air parcels from the central part of Chile (close to big cities such as Valparaíso and Santiago) rich in eBC are probably transported at the coastline northward by low-level mesoscale patterns (Rahn & Garreaud, 2014) after a forest fire episode, and due to regional circulation patterns at 30°S , described by Kalthoff, et al. (2002), the eBC is carried to the valleys and later on upward to TLL. However, if it happens the ozone produced by precursor gases emitted in the forest fires (Fujiwara, et al., 1999) must be affected by several transformations that remove ozone because low values are observed for this period at TLL.(figure 11).

The diurnal cycle of eBC shows high (low) concentrations during afternoon (morning) (figure 15). This pattern is also found in the diurnal cycle of ozone (figure 9) and suggests that ozone and eBC are correlated during this time and their associated air parcels come from the same place. The daily maxima and minima however differ by a few hours, so this hypothesis would need to be verified by an in-depth air mass modeling study.

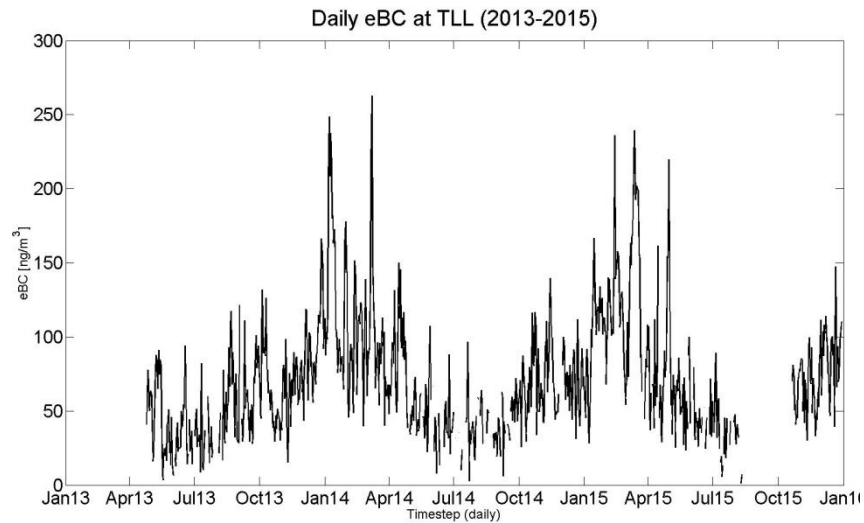


Figure 14. Daily series of eBC at TLL during 2013-2015.

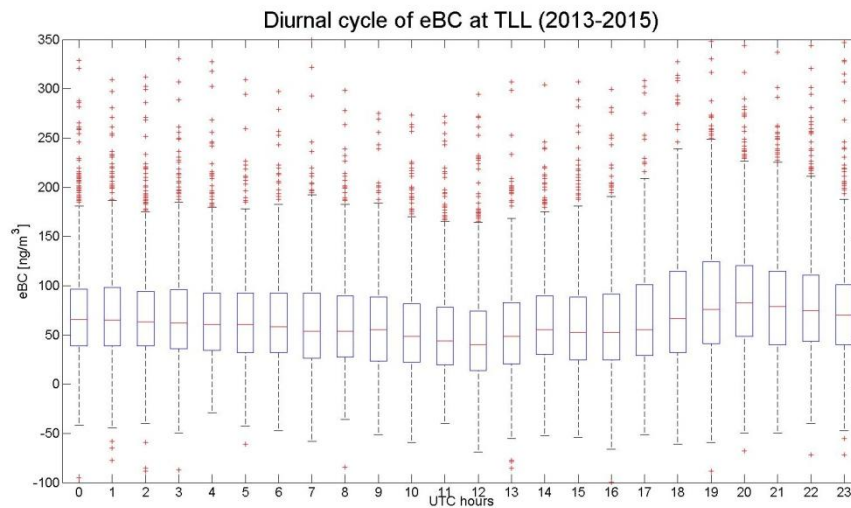


Figure 15. Boxplot, diurnal cycle of hourly eBC concentrations at TLL during 2013-2015. Top and bottom of boxes mean percentile 25 and 75 (p25 & p75, respectively), red line in box represents median value for each hour, extreme of top and bottom dashed lines represent $(2.5 \cdot p25 - 1.5 \cdot p75)$ and $(2.5 \cdot p75 - 1.5 \cdot p25)$, and red marker are taken as outliers.

The monthly series, as in the diurnal series, shows an annual cycle with maximal (minimal) values of eBC during summer and early autumn (winter). These high concentrations, as mentioned in the previous paragraph, could be due to more human activity in the surrounding valleys associated with vacation period (figures 16 and 17). Nevertheless, if summer values are extracted from the series and replaced by the annual mean, the monthly series of eBC more resemble the monthly series of ozone, which may be explained by the southern hemisphere biomass-burning. In addition, in the annual cycle the daily-concentration spread is much less during winter than other seasons (figure 17).

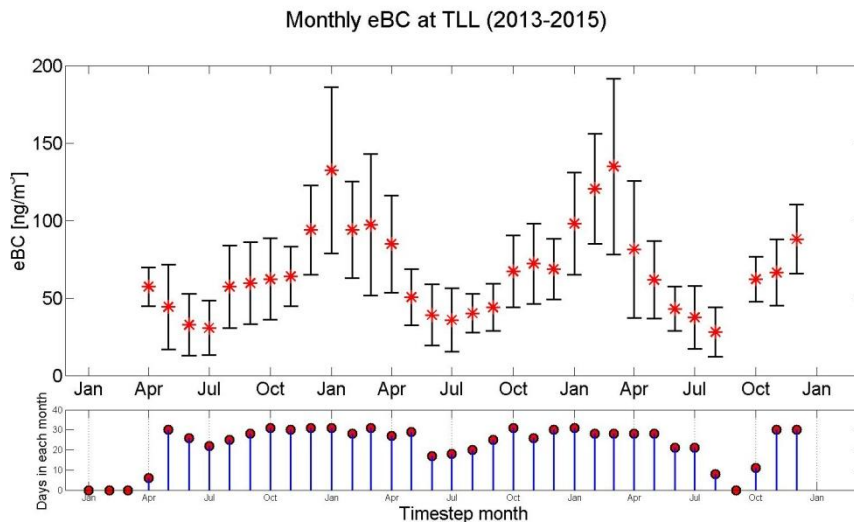


Figure 16. Top: monthly series of eBC concentrations at TLL during 2013-2015. Red markers represent average for each month, top and bottom black bars are one standard deviation each. Bottom: amount of daily averages in each month that are used to calculate monthly standard deviations and averages.

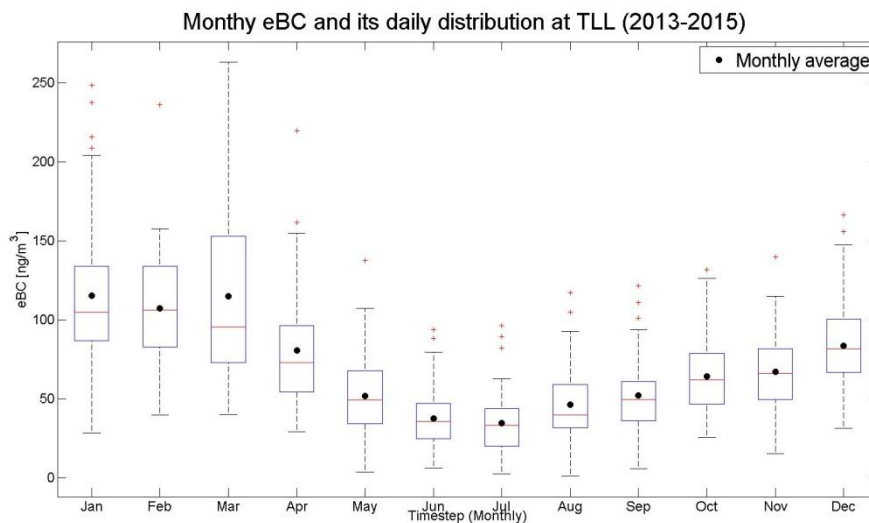


Figure 17. Boxplot, monthly cycle of daily eBC concentrations at TLL during 2013-2015. Top and bottom of boxes mean percentile 25 and 75 (p25 & p75, respectively), red line in box represents median value of each month, black markers mean average value of each month, extreme of top and bottom dashed lines represent $(2.5 \cdot p25 - 1.5 \cdot p75)$ and $(2.5 \cdot p75 - 1.5 \cdot p25)$, and red marker are taken as outliers.

3.1.4.- Angstrom Exponents

Fixed Gaussian distributions are observed in the AAE, SAE and SSAAE distributions (figure 18). AAE shows several hourly values between 1.0-1.5, which means that the hourly measurements of TLL site are influenced by aged diesel soot BC rather than biomass burning emissions. SAE exhibits large and fine particles at TLL. Large sized particles, likely dust, influence the zone as shown in the SAE distribution of the figure 1 (middle) with at least ca. 40% of values around and below 1, fine particles are approximately less than 10% of the data (SAE > 2), and the rest cannot be exactly defined. The arid conditions of the site are also confirmed by the SSAAE which illustrates at least 50% of the data below zero indicating the presence of dust. In other words, the ambient air at TLL is clearly influenced by dust and aged primary BC, which BC is also illustrated by the eBC amount in the section 3.1.3..

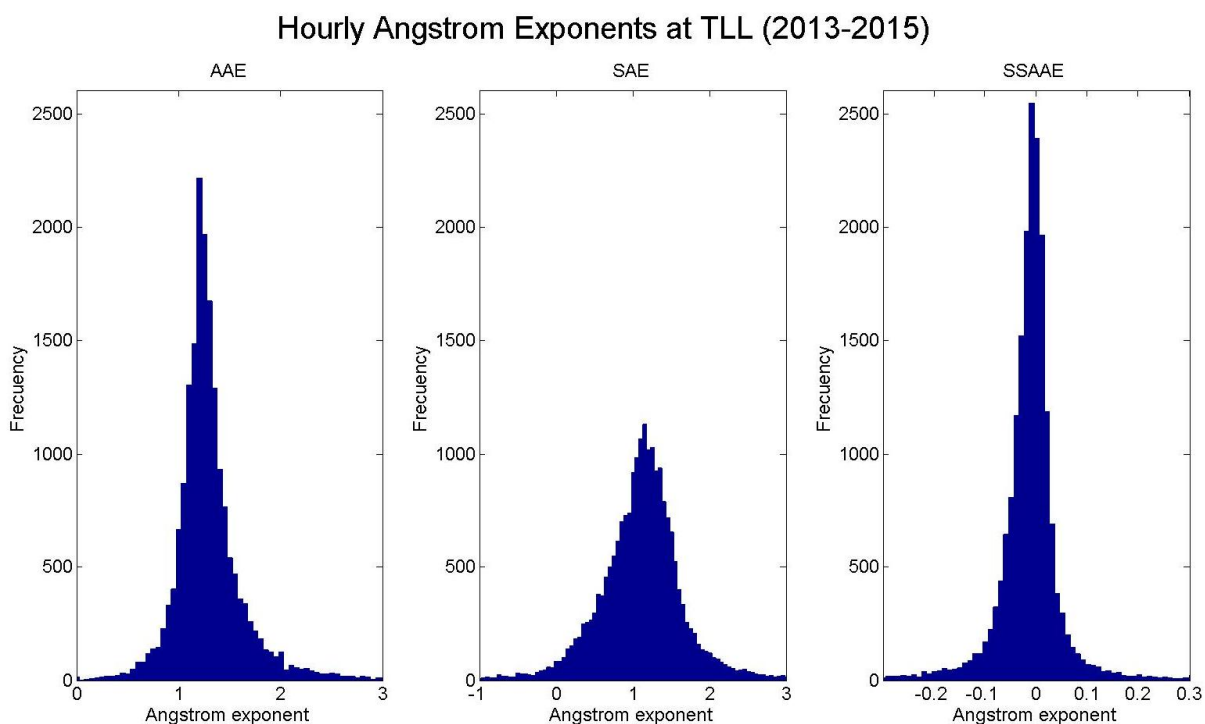


Figure 18. Hourly distribution at Cerro Tololo during 2013-2015. Top for AAE, middle SAE and bottom SSAAE.

No strong diurnal cycle is observed when analyzing hourly values (figure 19), nevertheless these values are consistent with the findings described in the previous paragraph, i.e. TLL is strongly influenced by dust and BC. During the local morning AAE spreads out reaching values of 1.5 (percentile 75, p75) with extreme values ($2.5 \cdot p75 - 1.5 \cdot p25$) around 2, which means that bio-mass/fuel-burning species are commonly found at TLL. The site is generally influenced by large-sized particles during the day, likely dust, which is demonstrated by low values of SAE and values below zero of SSAAE. But in several cases it is possible to see fine particles probably associated with BC (figure 19).

In general, daily AAE, SAE and SSAAE data present strong variability during 2013-2015 (figure 20). Four periods are selected to clarify relations between exponents. Episode A is called BC event because it shows fresh (pure) BC (AAE \rightarrow 1), fine and middle-sized particles (SAE

between 1.5-2), and no presence of dust (SSAAE > 0). Similarly, episode D shows same patterns but in longer temporal extension, although it probably includes a dust event in-between. In contrast, episode B is called dust event because it shows aged or biomass BC (AAE > 1.5), middle- and large-sized particles (SAE between 0-1), and presence of dust (SSAAE < 0). Similarly, episode C shows same patterns but in longer temporal extension (figure 20).

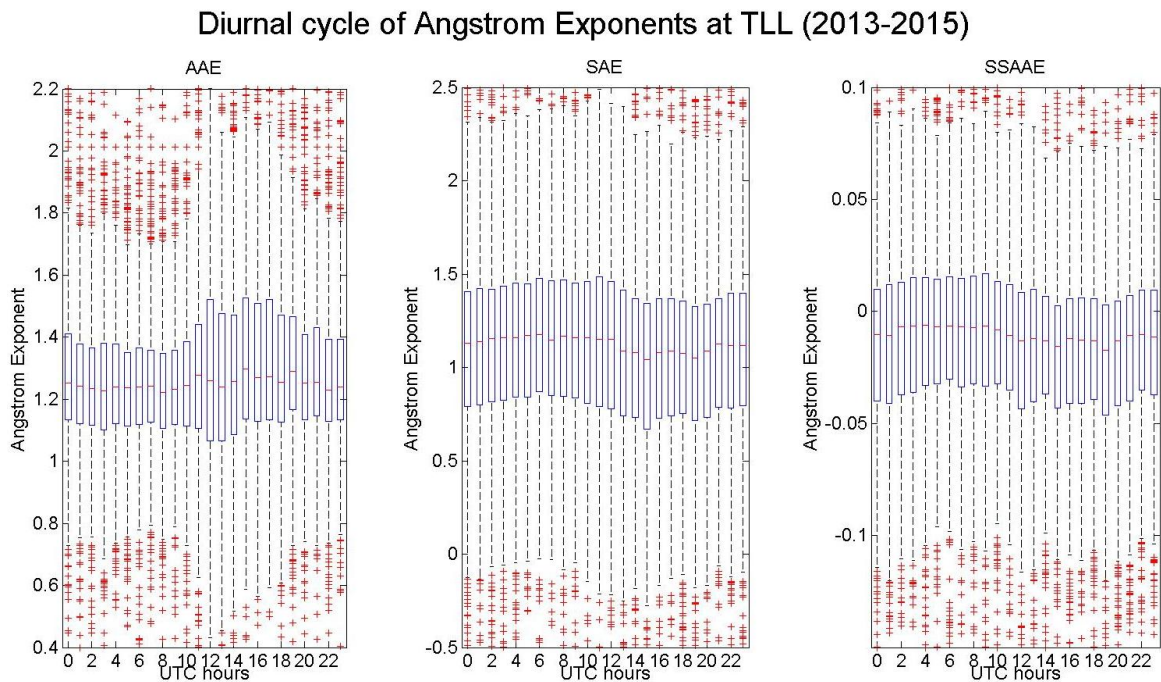


Figure 19. Boxplot, diurnal cycle of hourly Angstrom exponents at TLL during 2013-2015. Left for AAE, middle SAE and right SSAAE. Top and bottom of boxes mean percentile 25 and 75 (p25 & p75, respectively), red line in box represents median value for each hour, extreme of top and bottom dashed lines represent $(2.5 \cdot p25 - 1.5 \cdot p75)$ and $(2.5 \cdot p75 - 1.5 \cdot p25)$, and red marker are taken as outliers.

TLL presents dust most of the time which is confirmed by SSAAE. At the same time, TLL shows several episode no-dust where BC influences (figure 20 and 21). In addition, both type of aerosol can co-exist easily because dust always exists in the surrounding areas the year around and BC comes sometimes from human activity close to the site or in extreme events upward from the valleys and southern regions. Long-term events are also observed in the monthly series but no short-term event (figure 21).

Daily Angstrom Exponent

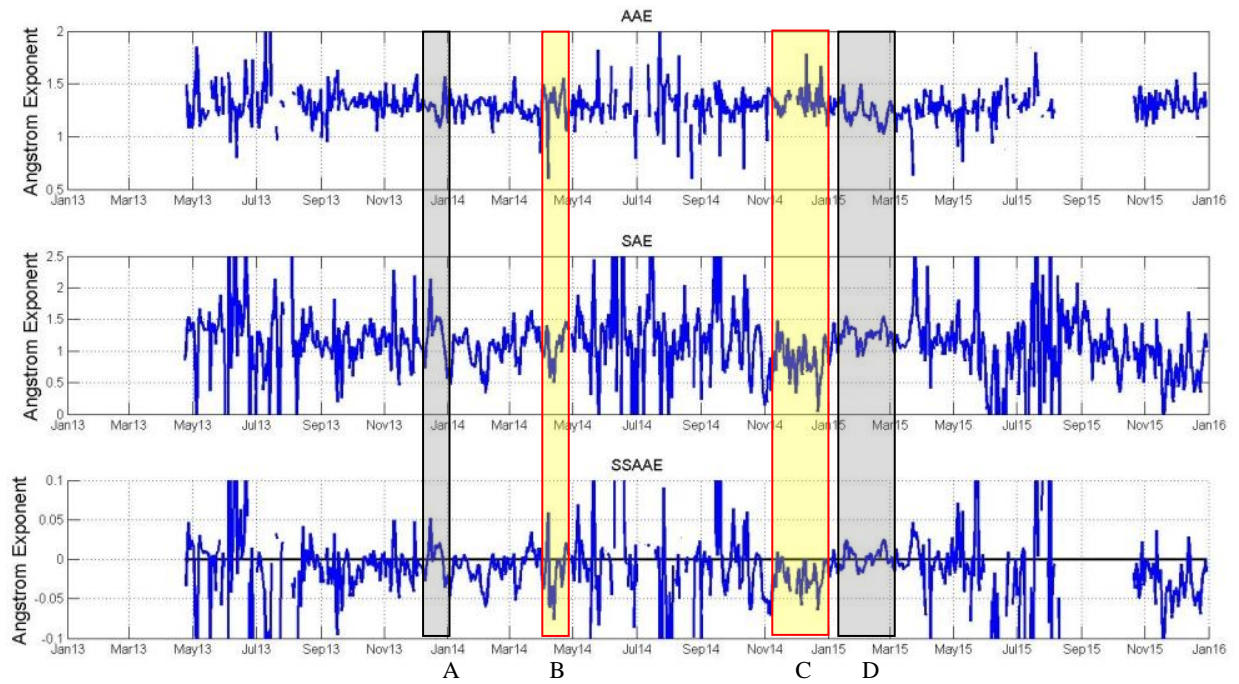


Figure 20. Time series of daily Angstrom Exponents at Cerro Tololo during 2013-2015. Top for AAE, middle SAE and bottom SSAAE. Black (yellow, B and C) zones represent BC (dust, A and D) episodes.

Monthly Angstrom Exponents

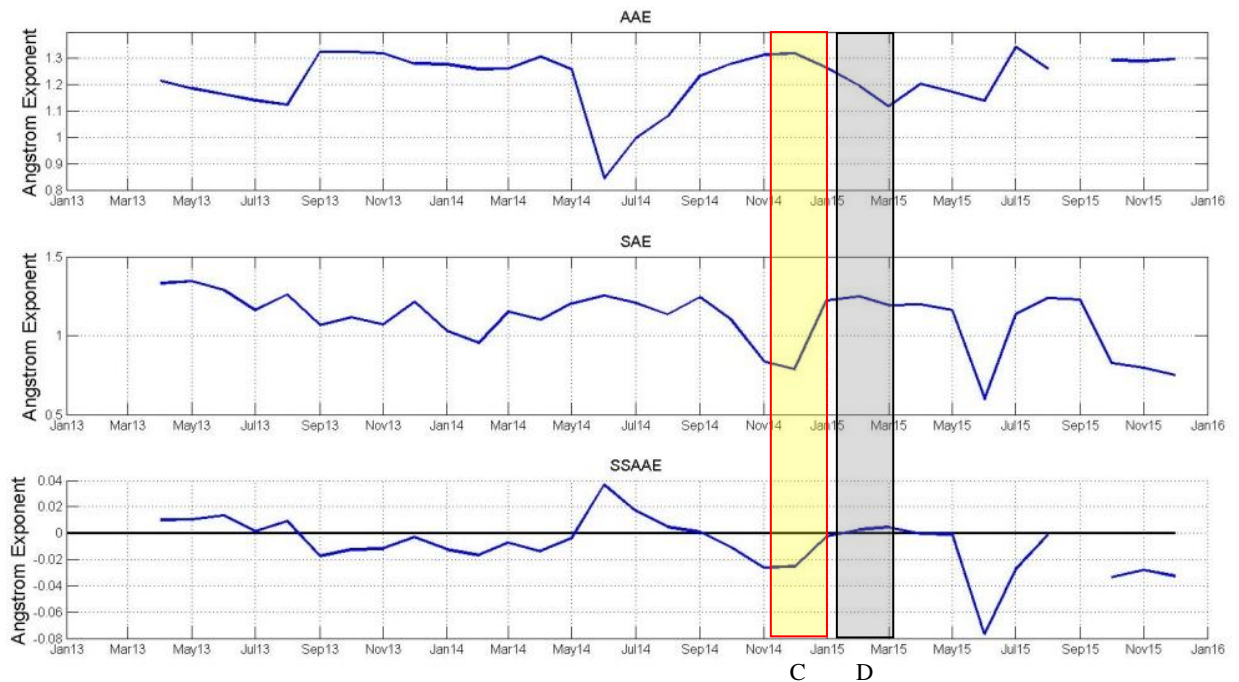


Figure 21. Monthly series of Angstrom Exponents at Cerro Tololo during 2013-2015. Top for AAE, middle SAE and bottom SSAAE. Black (yellow, C) zones represent BC (dust, D) episodes.

3.2.- Case Study

The dust index (SSAAE) has originally been used as a parameter to identify Saharan dust across Europe when it shows values below zero more than three hours (Coen et al., 2004). In this work we take the same concept and apply it to detect dust at TLL, most likely originated from the Atacama desert. In the case study presented in this section, SSAAE is calculated as daily average, one daily average below zero is used to identify a dust event. When the daily SSAAE shows that TLL is influenced by Dust, the daily events are selected and identified in the ozone, eBC and scattering coefficient daily time series.

On one hand, the dust cases (DU) are presented in the figure 22, which represents 50% of the entire period occurring the half of these events in summer (figure not shown). In addition, the year cycle of ozone and eBC for DU cases show similar patterns as found before in section 3.1.1. and 3.1.2. (figure 22, left & middle). Moreover, the $\sigma_{\text{scat}}(\lambda)$ separate from each other during summer (around 7 Mm^{-1}) indicating the presence of fine particles mostly associated with BC. In contrast, the separation of $\sigma_{\text{scat}}(\lambda)$ during winter is much less indicating likely presence of coarse particles associated with dust. The separation may also be a consequence of inverse $\sigma_{\text{scat}}(\lambda)$ pattern (red- top and blue-light bottom, 625 and 450 nm, respectively) in the daily values, which strongly indicates the presence of dust.

On the other hand, no dust cases (ND) are presented in the figure 23, which represents 25% of the entire period, and the rest 25% corresponds to not available values during 2013-2015. In addition, the year cycle of ozone and eBC for ND cases show the same patterns as found for DU cases. A clear and constant $\sigma_{\text{scat}}(\lambda)$ -separation of ND cases are observed through the year. This $\sigma_{\text{scat}}(\lambda)$ -separation confirms the no-presence (or less) of dust, consistent with ND cases.

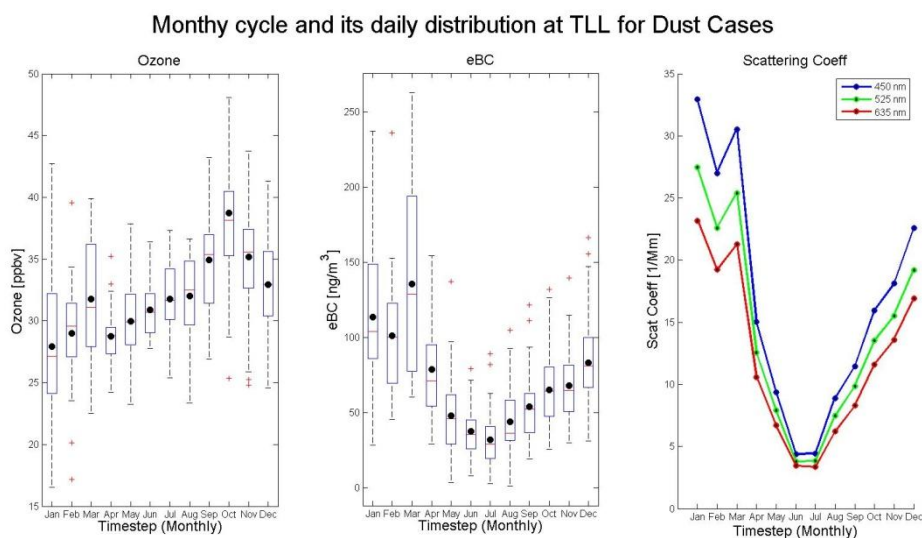


Figure 22. Monthly cycle at TLL for Dust Events: left represents boxplot of daily concentrations of ozone, middle boxplot of daily concentrations of eBC, and right monthly values of scattering coefficients.

Monthly cycle and its daily distribution at TLL for NO Dust Cases

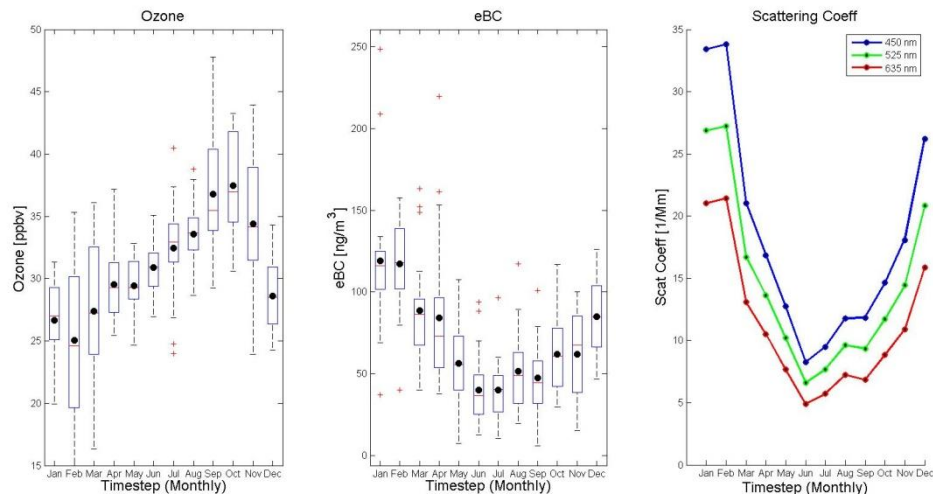


Figure 23. Monthly cycle at TLL for NO Dust Events: left represents boxplot of daily concentrations of ozone, middle boxplot of daily concentrations of eBC, and right monthly values of scattering coefficients.

In order to have a better look at randomly selected cases, four cases (2:DU & 2:ND) are analyzed in this section. The four selected cases are the March 7th 2014 and November 04th 2014 for DU cases, and the December 24th 2013 and May 05th 2015 for the ND case. In order to give a better view of the behavior pre and post event (± 12 days), figures henceforth present the day in the middle of the graph.

In the first DU case (March 07th, 2014) SSAE values below zero are observed 5 days before and 6 days after the event (figure 24, bottom), showing the strong influence of dust during the entire period. Additionally, eBC peaks on the event day (figure 25, bottom). Similarly, ozone shows the same pattern with an earlier increase and slower decrease (figure 25, top). This likely means that air parcels come from some polluted area, most likely urban area. In the days following the event, the increase in SSAE and SAE, along with the decrease in AAE, illustrated the diminishing influence of coarse mode dust particles..

The $\sigma_{\text{scat}}(\lambda)$ -separation is constant around 5 Mm⁻¹, which corresponds fairly well to the year-round separation found for dust cases only (figure 22). Finally, because TLL is most of the time over the marine boundary layer representing the free-atmosphere, fresh air (very low eBC and surface-ozone concentrations) is able to be observed 8 days after the event (figure 25), which comes from over the marine boundary layer at the coastline carrying probably some marine aerosols.

The second DU case (November 04th, 2014) represents a day in the middle of a strong dust period. SSAE values below zero are already observed 7 day before and 6 days after the event (figure 26, bottom). Moreover, large-sized aerosols (SAE around 0.2-0.6) and biomass burning (AAE around 1.4) are observed indicating either the co-existence of dust, BC and/or other aerosols (secondary organic aerosols) that have similar AAE values as biomass-BC (figure 26, top and middle).

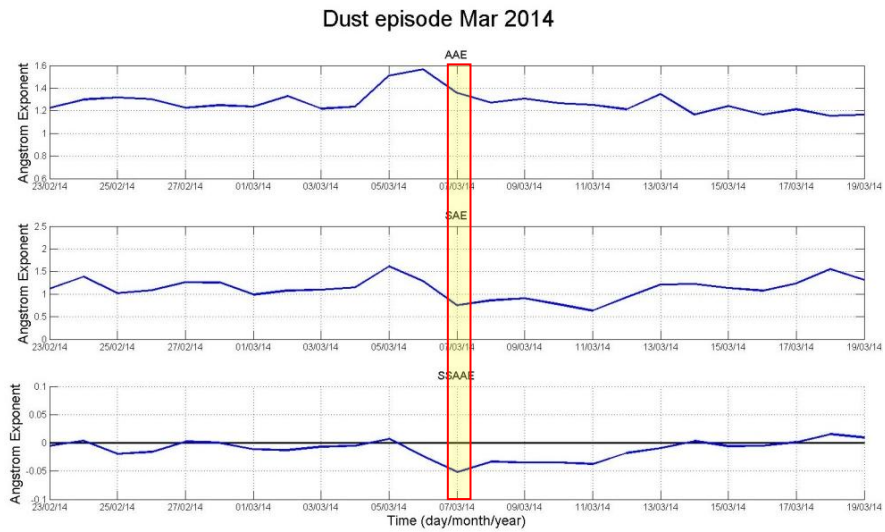


Figure 24. Dust case, 07/Mar/2014. Aerosol optical properties: top AAE, middle SAE, and bottom SSAAE. Yellow zone represents DU event.

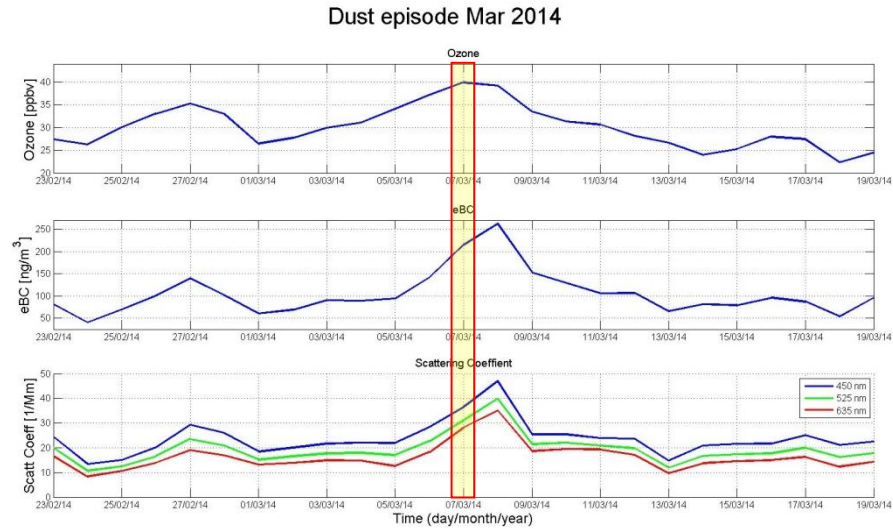


Figure 25. Dust case, 07/Mar/2014. Top ozone, bottom eBC, and bottom scattering coefficient. Yellow zone represents DU event.

In addition, low eBC values are observed 10 days before and after the event (figure 27, bottom). In contrast, ozone shows high values (figure 27, top) which means that air parcels come from upper level atmosphere, as described by Rondanelli et al. (2002). These parcels also bring dust particles lifted from hill peaks due to the upper-wind which is demonstrated by the collapsed $\sigma_{\text{scat}}(\lambda)$ -separation.

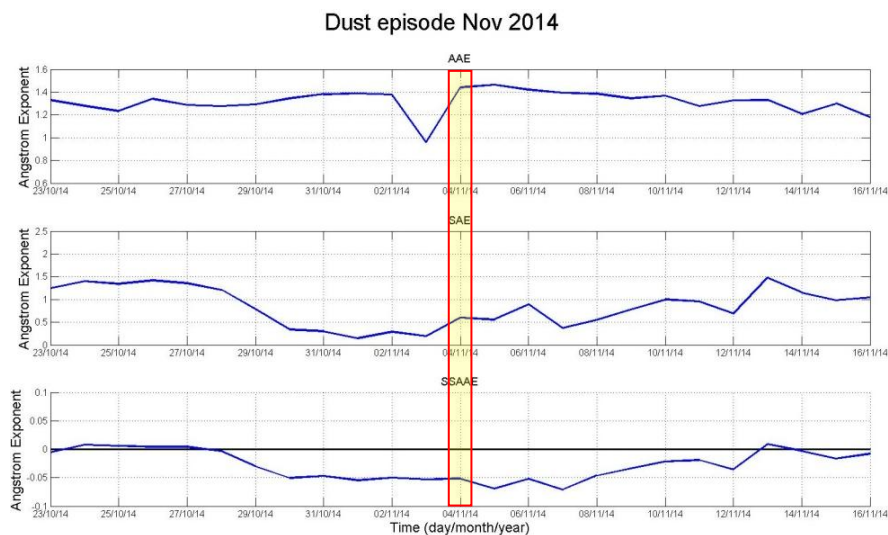


Figure 26. Dust case, 04/Nov/2014. Aerosol optical properties: top AAE, middle SAE, and bottom SSAAE. Yellow zone represents DU event.

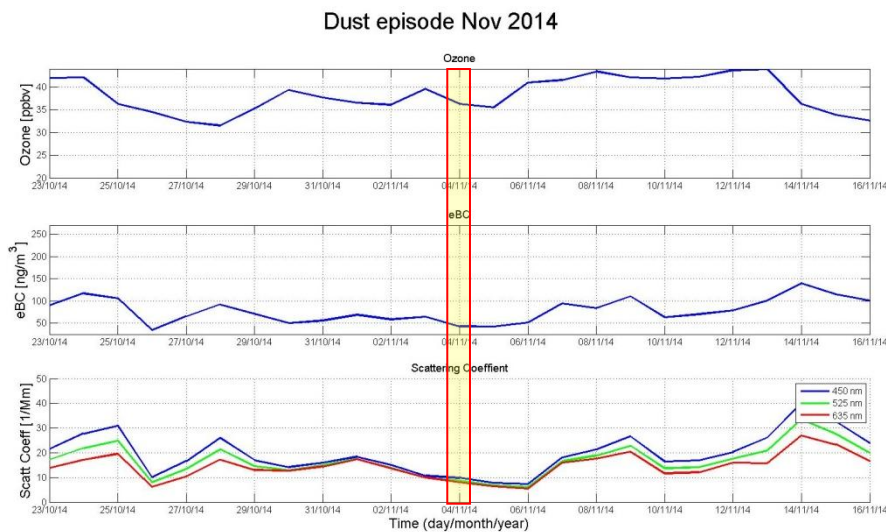


Figure 27. Dust case, 04/Nov/2014. Top ozone, bottom eBC, and bottom scattering coefficient. Yellow zone represents DU event.

In the first ND case (December 24th, 2013) SSAAE values over zero are observed 5 days before and 3 days after the event (figure 28, bottom). Middle-sized aerosols (SAE around 1.5) and fresh (pure) BC (AAE around 1) are observed, indicating the presence of aged BC particles linked to fuel burning (figure 28, top and middle). In addition, 3 days after the event a DU is observed showing higher AAE, associated with simultaneous biomass burning and coarse particles.

During the same event, eBC increase is already observed 2-3 days before the event lasting till 3-4 days after the event (figure 29, bottom). Similarly, ozone shows the same pattern as eBC with a decreasing-interruption between the event and 2 days after (figure 29, top). Decrease of both ozone and eBC 3 days after the event coincide with the presence of biomass burning and

dust as suggested by the AAE and SSAAE values (figure 28, top and bottom), respectively. In addition, 6 days after the event fresh air is observed (figure 29) which also carries some dust particles that are lifted from hill peaks due to the fresh-wind, demonstrated by the collapsed $\sigma_{\text{scat}}(\lambda)$ -separation.

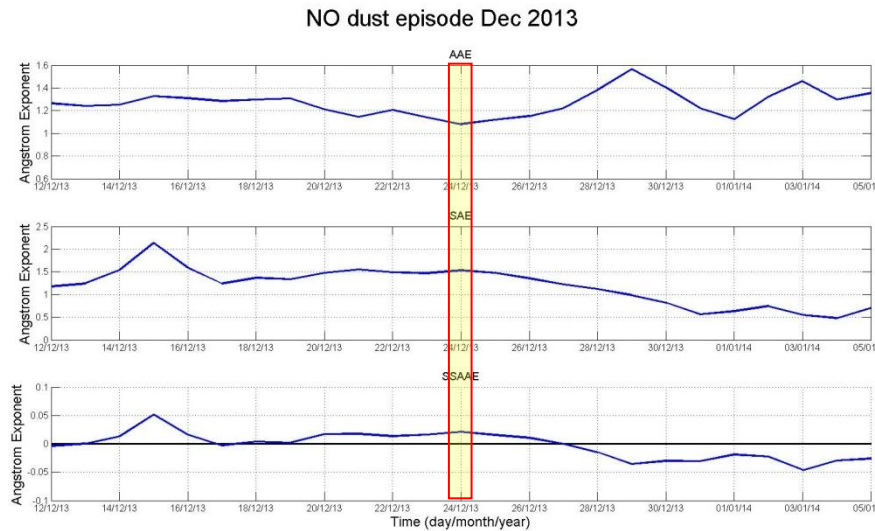


Figure 28. NO dust case, 24/Dec/2013. Aerosol optical properties: top AAE, middle SAE, and bottom SSAAE. Yellow zone represents ND event.

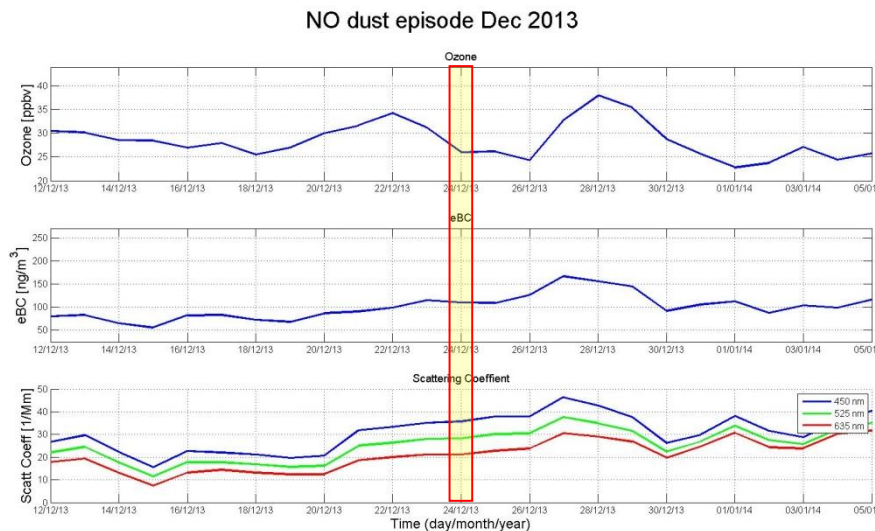


Figure 29. NO dust case, 24/Dec/2013. Top ozone, bottom eBC, and bottom scattering coefficient. Yellow zone represents ND event.

The second ND (May 05th, 2015) is a day in a series of consecutive days with changing dust influence. SSAAE values over zero are observed during the event and 5 days before and after the event (figure 30, bottom). Moreover, middle-sized aerosols (SAE around 1.5) and fresh (pure) BC (AAE around 1) are observed during the event indicating the presence of fuel burning related BC particles (figure 30, top and middle). In addition, the days between the event and 5

days later show dust with high AAE, commonly associated with biomass burning and coarse particles.

During the same event, decrease of eBC is observed 2 to 4 days before the event (figure 31, bottom). In contrast, ozone does not show any important change before and after the event (figure 31, top). AAE values around 1 are observed with almost no eBC and fresh air observed due to low values of ozone and eBC suggest that the very low amount of eBC present at the site is likely caused by local fuel burning.

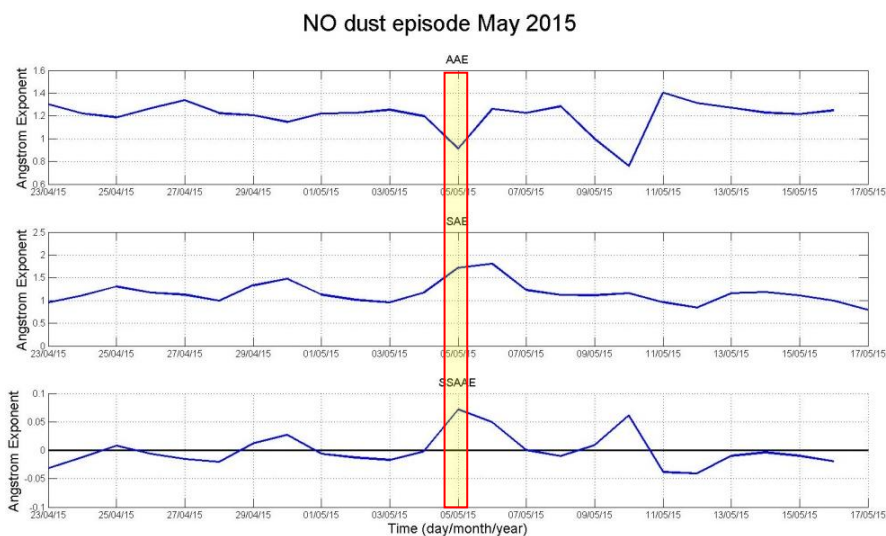


Figure 30. NO dust case, 05/May/2015. Aerosol optical properties: top AAE, middle SAE, and bottom SSAE. Yellow zone represents ND event.

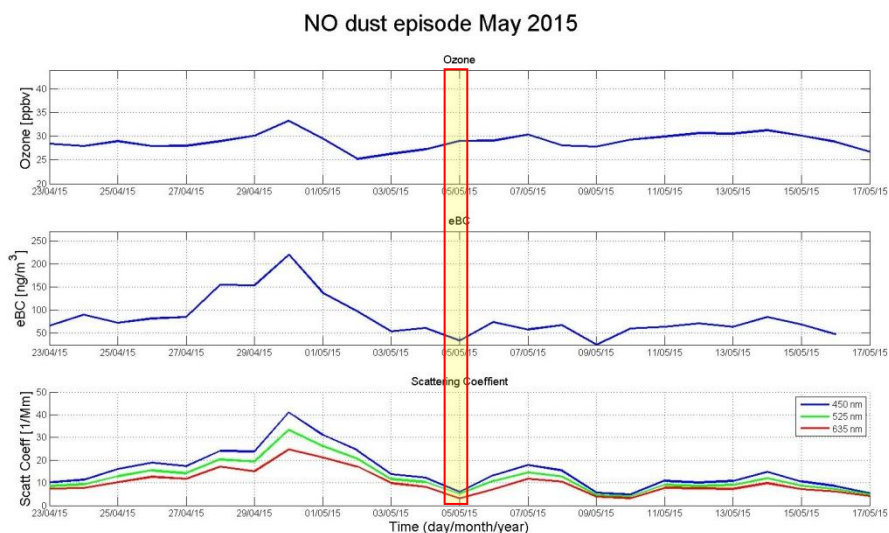


Figure 31. NO dust case, 05/May/2015. Top ozone, bottom eBC, and bottom scattering coefficient. Yellow zone represents ND event.

4.- Conclusions

The variability of ozone, equivalent black carbon and aerosol optical properties at Cerro Tololo during 2013-2015 are analyzed and described in this work. Furthermore, a dust parameter is used to define and discuss events that include ozone, equivalent black carbon and scattering coefficients.

Ozone shows high (low) concentrations during afternoon and night (morning), and maximal (minimum) concentrations during spring (summer). The monthly variability is linked to the biomass burning in the southern hemisphere. These variability patterns are consistent with the findings of Gallardo et al. (2000) and Rondanelli et al. (2002).

Equivalent black carbon shows the same diurnal pattern as ozone, and high (low) concentrations in summer (winter). On one hand, the monthly variability is probably related to the human activity in the surrounding areas which is higher in summer and early autumn due to school vacations, and lower in winter, not neglecting the possibility of deposition due to rain during rainy season (winter). If summer values are extracted from the series and replaced by the annual mean, the monthly series of eBC can seem like the monthly series of ozone, which may be explained by the southern hemisphere biomass-burning. On the other hand, high equivalent black carbon concentrations can also be linked to forest fires that occur in the same region or surrounding it during summer. However, the ozone produced by precursor gases emitted in the forest fires must be affected by several transformations that remove ozone because low values are observed for this period at Cerro Tololo.

Angstrom exponent distributions show a fixed Gaussian distribution. The hourly time series of the exponents show that Cerro Tololo is influenced by aged diesel soot black carbon rather than biomass burning emissions, and by large and fine particles. The arid conditions of the site are also confirmed by the single scattering albedo angstrom exponent which illustrates at least 50% of the data below zero indicating the presence of dust. In other words, the ambient air at Cerro Tololo is clearly influenced by dust and aged primary black carbon. Other relevant aerosol constituents (secondary organic and inorganic aerosols) are not measured at TLL and cannot be assessed by the available aerosol instrumentation.

Four periods are selected to clarify relations between exponents. Both types of aerosol can co-exist easily because dust always exists in the surrounding areas the year around, and black carbon comes probably from human activity close to the site or in extreme events upward from the valleys and southern regions.

In the dust cases ozone and equivalent black carbon show similar patterns as found in the short-climatology. Moreover, a distinct $\sigma_{\text{scat}}(\lambda)$ -separation indicates the domination of fine particles mostly associated with black carbon rather than dust particles, and opposite in winter the collapsed $\sigma_{\text{scat}}(\lambda)$ -separation probably indicates presence of coarse particles associated with dust. In contrast, in the no dust cases the monthly cycle of ozone, equivalent black carbon and the $\sigma_{\text{scat}}(\lambda)$ -separation have the same monthly patterns as found in the dust episodes. Nevertheless, the increase of the $\sigma_{\text{scat}}(\lambda)$ -separation confirms less or no presence of dust, as expected.

Four events are randomly selected and analyzed. The selected dust events indicate either the presence of dust and black carbon as well as ozone at the same time, or they suggest the

presence of other aerosol types that have similar single scattering albedo angstrom exponent values as biomass-black carbon. In the first dust event the air parcel likely comes from polluted areas and after 8 days from over the ocean. Beside the dust, the levels of eBC and ozone are high as well. In the second dust event the air parcel comes from upper level atmosphere (associated with low eBC values and high ozone values), as described by Rondanelli, et al. (2002), bringing dust particles probably lifted from hill peaks.

In the first no dust event the air parcel comes from some polluted area and after 6 days from over the ocean. The presence of black carbon particles linked to biomass burning is observed. In contrast, in the second no dust event the air parcel comes from over the ocean with no evidence of lifted dust particles, as opposed to the other events where the results suggest that fresh air parcels pick up dust on the way to TLL.

Air parcels coming from upper levels, over the ocean and polluted areas are observed at Cerro Tololo. These three types of parcels represent three types of transport mechanism. The first parcels represent stratosphere-troposphere interchange transport mostly associated with synoptic- and meso-scale meteorological patterns. The second parcels represent see-breeze likely enhanced by westerlies associated with meso-scale meteorological patterns. Finally, the third parcels represent local transport in the surrounding areas (valleys and inland) associated with meso- and local scale patterns.

Numerical simulations are necessary to clarify air-parcel origins. Moreover, additional instruments measuring specific type of aerosols are considered a very important help identifying the source. Both the instruments and the numerical simulations may describe much better the transport mechanisms that influence the region of Cerro Tololo. Nevertheless, meteorological stations are required to validate the products of the simulations. The next step is to validate the meteorological data that exist at Cerro Tololo, which will help validating the model outputs.

5.- Bibliography.

- Andreae, M. O., & Gelencsér, A. (2006). Black carbon or brown carbon? The nature of light-absorbing carbonaceous aerosols. *Atmospheric Chemistry and Physics*, 6(10), 3131-3148.
- Artaxo, P., Oyola, P., & Martinez, R. (1999). Aerosol composition and source apportionment in Santiago de Chile. *Nuclear Instruments and Methods in Physics Research Section B: Beam Interactions with Materials and Atoms*, 150(1), 409-416.
- Bond, T. C., & Bergstrom, R. W. (2006). Light Absorption by Carbonaceous Particles: An investigate Review. *Aerosol science and technology*, 40(1), 27-67.
- Bond, T. C., Anderson, T. L., & Campbell, D. (1999). Calibration and intercomparison of filter-based measurements of visible light absorption by aerosols. *Aerosol science and technology*, 30(6), 582-600.
- Bond, T. C., Doherty, S. J., Fahey, D. W., Forster, P. M., Berntsen, T., DeAngelo, B. J., . . . Zender, C. S. (2013). Bounding the role of black carbon in the climate system: A. *Journal of geophysical research*, 118, 5380-5552.
- Brook, R. D., Brook, J. R., & Rajagopalan, S. (2003). Air pollution: the "Heart" of the problem. *Current hypertension reports*, 5(1), 32-39.
- Brunekreff, B., & Holgate, S. (2002). Air pollution and health. *The lancet*, 360, 1233-1242.
- Ching, J., Riemer, N., & West, M. (2016). Black Carbon mixing state impacts on cloud microphysical properties: Effects of aerosol plume and enviromental conditions. *Journal of Geophysical Research: Atmospheres*.
- Chung, C., Ramanathan, V., Kim, D., & Podgorny, I. (2005). Global anthropogenic. *Journal of Geophysical Research*, 10(D24), D24207.
- Coen, M. C., Weingartner, E., Schaub, D., Hueglin, C., Corrigan, C., Henning, S., . . . Baltensperger, U. (2004). Saharan dust events at the Jungfrauoch: Detection by wavelength dependence of the single scattering albedo and first climatology analysis. *Atmospheric chemistry and physics*, 4, 2465-2480.
- Collaud Coen, M., Weingartner, E., Schaub, D., Hueglin, C., Corrigan, C., Henning, S., . . . Baltensperger, U. (2004). Saharan dust events at the Jungfrauoch: Detection by wavelength dependence of the single scattering albedo and first climatology analysis. *Atmospheric chemistry and physics*, 4, 2465-2480.
- CONAF. (2015, 07). *Incendios Forestales - Estadísticas Históricas*. Retrieved 06 29, 2016, from Ministerio de Agricultura de Chile: <http://www.conaf.cl/incendios-forestales/incendios-forestales-en-chile/estadisticas-historicas/>
- Crutzen, P. (1995). Ozone in the troposphere. . *Composition, chemistry, and climate of the atmosphere*, 349-393.
- DeCarlo, P. F., Dunlea, E. J., Kimmel, J. R., Aiken, A. C., Sueper, D., Crounse, J., . . . Jimenez, J. L. (2008). Fast airborne aerosol size and chemistry measurements above Mexico City and Central Mexico during the MILAGRO campaign. *Atmospheric chemistry and physics*, 8, 4027-4048.
- Donoian, H. C., & Medalia, A. I. (1967). Scattering and absorption of light by carbon black. *J. Paint Technol*, 39(515), 716-728.
- Duncan, B. M., Martin, R. V., Sautd, A. C., Yevich, R., & Logan, J. A. (2003). Interannual and seasonal variability of biomass burning emissions constrained by satellite observations. *Journal of Geophysical Research*, 108(D2).
- Finlayson-Pitts, B. J., & Pitts Jr., J. N. (1999). *Chemistry of the upper and lower atmosphere theory, experiments, and applications*. Academic press.

- Fuenzalida, H., Sánchez, R., & Garreaud, R. (2005). A climatology of cutoff lows in the Southern Hemisphere. *Journal of Geophysical Research: Atmospheres*, 110(D18).
- Fujiwara, M., Kita, K., Kawakami, S., Ogawa, T., Komala, N., Saraspriya, S., & Surtipito, A. (1999). Tropospheric ozone enhancements during the Indonesian forest fire events in 1994 and in 1997 as revealed by ground-based observations. *Geophysical Research Letters*, 26(16), 2417-2420.
- Fuller, K. A., Malm, W. C., & Kreidenweis, S. M. (1999). Effects of mixing on extinction by carbonaceous particles. *Journal of geophysical research*, 104(15), 941-954.
- Gallardo, L., Carrasco, J., & Olivares, G. (2000). An analysis of ozone measurements at Cerro Tololo (30 degrees S, 70 degrees W, 2200 m.a.s.l.) in Chile.. *Tellus Series B-Chemical and Physical Meteorology*, 52, 50-59.
- Goldberg, S. (1986). Chemical modeling of arsenate adsorption on aluminum and iron oxide minerals. *Soil Science Society of America Journal*, 50(5), 1154-1157.
- Haywood, J., & Boucher, O. (2000). Estimates of the direct and indirect radiative forcing due to tropospheric aerosols: A review. *Reviews of geophysics*, 38(4), 513-543.
- Herrmann, E., Weingartner, E., Bukowiecki, N., Hammer, E., Collaud Coen, M., Conen, F., . . . Baltensperger, U. (2014). An aerosol climatology for the Jungfrauoch Part 1: Criteria for cloud presence and boundary layer influence. *EGU General Assembly Conference Abstracts*, 16(11698).
- Holben, B., Tandr , D., Smirnov, A., Eck, T., Slutsker, I., Abuhassan, N., . . . Zibordi, G. (2001). An emerging ground-based aerosol climatology: Aerosol optical depth from AERONET. *Journal of Geophysical Research*, 106(D11), 12067-12097.
- Holton, J., & Hakim, G. (2013). An introduction to dynamic meteorology. *Academic press*.
- Horvath, H. (1993b). Comparison of measurements of aerosol optical absorption by filter collection and a transmissometric method. *Atmospheric Environment. Part A. General Topics*, 27(3), 319-325.
- Kalthoff, N., Bischoff-Gauss, I., Fliebig-Wittmaack, M., Fiedler, F., Th rauf, J., Novoa, E., . . . Kohler, M. (2002). Mesoscale Wind Regimes in Chile at 30 S. *Journal of applied Meteorology*, 41(9), 953-970.
- Kennedy, I. M. (2007). The health effects of combustion-generated aerosols. *Proceedings of the Combustion Institute*, 31(2), 2757-2770.
- Kim, J., Bauer, H., Dobovicnik, T., Hitzenberger, R., Lottin, D., Ferry, D., & Petzold, A. (2012). Constraining optical properties and refractive index of soot through combined experimental and modelling studies. *European Aerosol Conference (EAC), September 2012.*, (pp. 2-7). Granada, Spain.
- Kirchstetter, T. W., Novakov, T., & Hobbs, P. V. (2004). Evidence that the spectral dependence of light absorption by aerosols is affected by organic carbon. *Journal of Geophysical Research: Atmosphere*, 109(D21).
- Knox, A., Evans, G. J., Brook, J. R., Yao, X., Jeong, C. -H., Godri, K. J., . . . Slowik, J. G. (2009). Mass absorption cross-section of ambient black carbon aerosol in relation to chemical age. *Aerosol science and technology*, 43(6), 522-532.
- Lei, Y. C., Hwang, J. S., Chan, C. C., Lee, C. T., & Cheng, T. J. (2005). Enhanced oxidative stress and endothelial dysfunction in streptozotocin-diabetic rats exposed to fine particles. *Environmental research*, 99(3), 335-343.
- Lenoble, J., Remer, L., & Tanr , D. (Eds.). (2013). *Aerosol Remote Sensing*. Springer Science & Business Media.
- Mahrer, Y., & Pielke, R. (1977). The effects of topography on sea and land breezes in a two-dimensional numerical model. *Monthly weather review*, 105, 1151-1162.

- Miller, A. (1976). Climates of Central and South America: The Climate of Chile. In *World Survey of Climatology* (Vol. 12, pp. 113-147). New York: Elsevier Sci.
- Montecinos, S., Gutiérrez, J. R., López-Cortés, F., & López, D. (2016). Climatic characteristics of the semi-arid Coquimbo Region in Chile. *Journal of Arid Environments*, 126, 7-11.
- Morata, D., Polvé, M., Valdés, A., Belmar, M., Dinator, M. I., Silva, M., . . . Morales, J. R. (2008). Characterisation of aerosol from Santiago, Chile: an integrated PIXE-SEM-EDX study. *Environmental Geology*, 56(1), 81-95.
- Müller, G., Artz, R., Baltensperfer, U., Carmichael, G., Dlugokencky, E., Penkett, S., . . . Nickovic, S. (2007). WMO Global Atmosphere Watch (GAW) Strategic Plan: 2008-2015. *World Meteorological Organization, Geneva, GAW Report*(172), p. 104.
- Müller, T., Henzing, J. S., de Leeuw, G., Wiedensohler, A., Alastuey, A., Angelov, H., . . . Wang, Y. Q. (2011). Characterization and intercomparison of aerosol absorption photometers: result of two intercomparison workshops. *Atmospheric Measurement Techniques*, 4(2), 245-268.
- NASA. (2010). *Earth Observatory*. Retrieved 06 20, 2016, from Aerosols: Tiny Particles, Big Impact.: <http://earthobservatory.nasa.gov/Features/Aerosols/>
- Ogren, J., & Charlson, R. (1983). Elemental carbon in the atmosphere: cycle and lifetime. *Tellus B*, 35B(4), 241-254.
- Oltmans, S., Lefohn, A., Harris, J., Galbally, I., Scheel, H., Bodeker, G., . . . Simmonds, P. (2006). Long-term changes in tropospheric ozone. *Atmospheric Environment*, 40(17), 3156-3173.
- Organization, W., & Europe, W. (2006). *Air quality guidelines: global update 2005: particular matter, ozone, nitrogen dioxide, and sulfur dioxide*, World Health Organization.
- Paris 2015 UN Climate Change Conference COP21 - CMP11. (n.d.). Retrieved 06 16, 2016, from <http://www.cop21.gouv.fr/en/>
- Penner, J. E., Andreae, M., Annegarn, H., Barrie, L., Feichter, J., Hegg, D., . . . Pitari, G. (2001). Aerosols, their direct and indirect effects. In *Climate Change 2001: The Scientific Basis. Contribution of Working Group I to the Third Assessment Report of the Intergovernmental Panel on Climate Change (IPCC)* (pp. 289-348). Cambridge University Press.
- Petters, M. D., & Kreidenweis, S. M. (2007). A single parameter representation of hygroscopic growth and cloud condensation nucleus activity. *Atmospheric Chemistry and Physics*, 7(8), 1961-1971.
- Petzold, A., Kopp, C., & Niessner, R. (1997). The dependence of the specific attenuation cross-section on black carbon mass fraction and particle size. *Atmospheric Environment*, 31(5), 661-672.
- Petzold, A., Ogren, J. A., Fiebig, M., Laj, P., Li, S. M., Baltensperger, U., . . . Zhang, X. -Y. (2013). Recommendations for reporting "black carbon" measurements. *Atmospheric Chemistry and Physics*, 13(16), 8365-8379.
- Petzold, A., Rasp, K., Weinzierl, B., Esselborn, M., Hamburger, T., Dörnbrack, A., . . . Virkkula, A. (2009). Saharan dust absorption and refractive index from aircraft-based observations during SAMUM 2006. *Tellus B*, 61(1), 118-130.
- Petzold, A., Veira, A., Mund, S., Esselborn, M., Kiemle, C., Weinzierl, B., . . . Kandler, K. (2011). Mixing of mineral dust with urban pollution aerosol over Dakar (Senegal): impact on dust physico-chemical radiative properties. *Tellus B*, 63(4), 619-634.
- Pizarro, J. G., & Montecinos, A. (2000). Cutoff cyclones off the subtropical coast of Chile. Preprints. *Sixth International Conference on Southern Hemisphere Meteorology and Oceanography*, (pp. 278-279). Santiago de Chile.

- Pope III, C. A., Burnett, R. T., Thun, M. J., Calle, E. E., Krewski, D., Ito, K., & Thurston, G. D. (2002). Lung cancer, cardiopulmonary mortality, and long-term exposure to fine particulate air pollution. *Jama*, 287(9), 1132-1141.
- Pope III, C. A., Thun, M. J., Namboodiri, M. M., Dockery, D. W., Evans, J. S., Speizer, F. E., & Heath Jr., C. W. (1995). Particulate air pollution as a predictor of mortality in a prospective study of US adults. *American journal of respiratory and critical care medicine*, 151(3_pt_1), 669-674.
- Proietti, E., Rössli, M., Frey, U., & Latzin, P. (2013). Air pollution during pregnancy and neonatal outcome: a review. *Journal of aerosol medicine and pulmonary drug delivery*, 26(1), 9-23.
- Rahn, D. A., & Garreaud, R. D. (2014). A synoptic climatology of the near-surface wind along the west coast of South America. *International Journal of Climatology*, 34(3), 780-792.
- Rai, P. K. (2016). Impacts of particulate matter pollution on plants: Implications for environmental biomonitoring. *Ecotoxicology and environmental safety*, 129, 120-136.
- Rondanelli, R., Gallardo, L., & Garreaud, R. (2002). Rapid changes in ozone mixing ratios at Cerro Tololo (30°10' S, 70° 48' W, 2200 m) in connection with cutoff lows and deep troughs. *Journal of Geophysical Research: Atmospheres*, 107(D23).
- Russel, P. B., Bergstrom, R. W., Shinozuka, Y., Clarke, A. D., DeCarlo, P. F., Jimenez, J. L., . . . Strawa, A. (2010). Absorption Angstrom Exponent in AERONET and related data as an indicator of aerosol composition. *Atmospheric chemistry and physics*, 10, 1155-1169.
- Rutllant, J., & Fuenzalida, H. (1991). Synoptic aspects of the central Chile rainfall variability associated with the Southern Oscillation. *International Journal of Climatology*, 11(1), 63-76.
- Sasser, E., Hemby, J., Adler, K., Anenberg, S., Bailey, C., & ... (2012). *Report to Congress on Black Carbon*. US Environmental Protection Agency, Washington, DC, USA.
- Schnaiter, M., Gimmler, M., Llamas, I., Linke, C., Jäger, C., & Mutschke, H. (2006). Strong spectral dependence of light absorption by organic carbon particles formed by propane combustion. *Atmospheric Chemistry and Physics*, 6(10), 2981-2990.
- Seinfeld, J., & Pandis, S. (2012). *Atmospheric chemistry and physics: from air pollution to climate change*. John Wiley & Sons.
- Shao, Y. (2008). *Physics and modelling of wind erosion* (Vol. 37). Springer Science & Business Media.
- Shinozuka, Y., Clarke, A. D., DeCarlo, P. F., Jimenez, J. L., Dunlea, E. J., Roberts, G. C., . . . Zhou, J. (2009). Aerosol optical properties relevant to regional remote sensing of CCN activity and links to their organics mass fraction: airborne observations over Central Mexico and US West Coast during MILAGRO/INTEX-B. *Atmospheric chemistry and physics*, 9, 6727-6742.
- Shinozuka, Y., Clarke, A., Howell, S., & al., e. (2008). Relations between cloud condensation nuclei and aerosol optical properties relevant to remote sensing: airborne measurements in biomass burning, pollution and dust aerosol over North America, *Eos trans. AGU*, 89(53), Abstract A41E-0164.
- Škerlak, B., Sprenger, M., & Wernli, H. (2014). A global climatology of stratosphere-troposphere exchange using the ERA-Interim data set from 1979 to 2011. *Atmospheric Chemistry and Physics*, 14, 913-937.
- Stier, P., Seinfeld, J., Kinne, S., Boucher, & Boucher, O. (2007). Aerosol absorption and radiative forcing. *Atmospheric Chemistry and Physics*, 7(19), 5237-5261.
- Stocker, T. F., Qin, D., Plattner, G. K., Tignor, M., Allen, S. K., Boschung, J., . . . Midgley, B. M. (2013). IPCC, 2013: climate change 2013: the physical science basis: Working Group I

- contribution to the Fifth assessment report of the Intergovernmental Panel on Climate Change.
- Tilmes, S., Lamarque, J., Emmons, L., Conley, A., Schultz, M., & co-authors. (2011). Ozonesonde climatology between 1995 and 2009: description, evaluation and applications. *Atmospheric Chemistry and Physics Discussions*, *11*, 28747-28796.
- Tilmes, S., Lamarque, J., Emmons, L., Conley, A., Schultz, M., & co-authors. (2012). Technical Note: Ozonesonde climatology between 1995 and 2011: description, evaluation and applications. *Atmospheric Chemistry and Physics*, *12*, 7475-7497.
- UNEP/WMO. (2011). *Integrated Assessment of Black Carbon and Tropospheric Ozone*. UNEP and WMO, Geneva, Switzerland.
- Wilks, D. S. (2011). *Statistical methods in the atmospheric sciences* (Vol. 100). Academic press.
- WMO/GAW. (2011). WMO Global Atmosphere Watch (GAW) Strategic Plan:2008-2015. *World Meteorological Organization*.
- Yang, S., Xu, B., Cao, J., Zender, C. S., & Wang, M. (2015). Climate effect of black carbon aerosol in a Tibetan Plateau glacier. *Atmospheric Environment*, *111*, 71-78.
- Zieger, P., Kienast-Sjögren, E., Starace, M., von Bismarck, J., Bukowiecki, N., Baltensperger, U., . . . Weingartner, E. (2012). Spatial variation of aerosol optical properties around the high-alpine site Jungfraujoch (3580 m.a.s.l.). *Atmospheric chemistry and physics*, *12*(15), 7231-7249.
- Ziemke, J., Chandra, S., Labow, G., Bhartia, P., Froidevaux, L., & co-authors. (2011). A global climatology of atmospheric and stratospheric ozone derived from Aura OMI and MLS measurements. *Atmospheric Chemistry and Physics*, *11*, 9237-9251.

Appendix A - List of abbreviations

AAE	Absorption Angstrom Exponent
BC	Black Carbon
DMC	Dirección Meteorológica de Chile
DU	Dust (event)
EBC	Equivalent Black Carbon
GAW	Global Atmospheric Watch Program
GHG	Greenhouse Gas
LAC	Light-Absorbing Carbonaceous
MAC	Mass Absorption Cross-section
ND	No Dust (event)
SAE	Scattering Angstrom Exponent
SSAAE	Single Scattering Albedo Angstrom Exponent
STJ	Subtropical Jet Stream
TLL	Cerro Tololo
UTC	Universal Time Coordinated
WMO	World Meteorological Organization
$\sigma_{abs}(\lambda)$	Absorption Coefficient
$\sigma_{ext}(\lambda)$	Extinction Coefficient
$\sigma_{scat}(\lambda)$	Scattering Coefficient